Journal of Computational Physics 230 (2011) 6756–6777

Contents lists available at ScienceDirect

Journal of Computational Physics

journal homepage: www.elsevier.com/locate/jcp

A nonlinear PSE method for two-fluid shear flows with complex interfacial topology

Lawrence C. Cheung, Tamer A. Zaki *

Department of Mechanical Engineering, Imperial College London, Exhibition Road, London SW7 2AZ, United Kingdom

ARTICLE INFO

Article history:
Received 18 July 2010
Received in revised form 9 May 2011
Accepted 12 May 2011
Available online 20 May 2011

Keywords:
Nonlinear instability
Parabolized stability equations
Two-fluid shear flows
Interfacial waves

ABSTRACT

A nonlinear stability method is developed for laminar two-fluid shear flows which undergo changes in the interface topology. The method is based on the nonlinear parabolized stability equations (PSE) and incorporates a scalar-based interface capturing (IC) scheme in order to track complex deformations of the fluid interface. In doing so, the formulation retains the flexibility and physical insight of instability-wave based methods, while providing hydrodynamic modeling capabilities similar to direct numerical calculations: the new formulation, referred to as the IC-PSE, can capture the nonlinear physical mechanisms responsible for generating large-scale, two-fluid structures, without incurring heavy computational costs. This approach is valid for spatially developing, laminar two-fluid shear flows which are convectively unstable, and can naturally account for the growth of finite amplitude interfacial waves, along with changes to the interfacial topology. We demonstrate the accuracy of the IC-PSE against direct Navier–Stokes calculations for two-fluid mixing layers with density and viscosity stratification. The comparisons show that the IC-PSE can predict the dynamics of the instability waves and capture the formation of Kelvin–Helmholtz vortex rolls and large scale liquid structures, at an order of magnitude less computational cost than direct calculations. The role of surface tension in the IC-PSE formulation is shown to be valid for flows in which $\mathrm{Re}/\mathrm{We} \lesssim 1$, and the method accurately predicts the formation and non-linear evolution of flow structures in this limit. This is demonstrated for spatially developing mixing layers which lead to vortex roll-up and ligaments, prior to droplet formation. The pinch-off process itself is a high surface tension phenomenon and in not considered herein. The method also accurately captures the effect of interfacial waves on the mean flow, and the topology changes during the non-linear evolution of the two-fluid structures.

1. Introduction

In many engineering applications involving two-fluid shear flows, the ability to track the growth of interfacial instability waves from their initial appearance to the formation of large-scale, coherent structures is highly desirable. For instance, in capillary jet flows or gas–liquid flows through pipelines, the formation of ligaments on the liquid surface directly affects the process by which liquid is entrained into the bulk flow. In order to accurately capture these structures, both the nonlinear dynamics of the instability waves and the complex deformations of the interface must be properly resolved. Current theoretical or computational tools, such as linear stability theory, are limited in the scope of their applicability, or in the case of direct simulations, can be too computationally expensive to apply on a casual basis.

* Corresponding author. Tel.: +44 (0) 20 7594 7032.
E-mail addresses: cheung@ge.com (L.C. Cheung), t.zaki@imperial.ac.uk (T.A. Zaki).

0021-9991/$ - see front matter © 2011 Elsevier Inc. All rights reserved.
doi:10.1016/j.jcp.2011.05.007

The objective of the current work is to develop a computational method which harnesses the insight and efficiency of stability methods, and the accuracy of direct computations. This approach borrows several ideas from instability wave theory and recent work on interface tracking to yield a nonlinear formulation which can be applied to study the dynamics of large-scale, two-fluid structures. By coupling the parabolized stability equations (PSE) with a scalar-based interface capturing scheme, the formulation is ultimately capable of predicting the development of small-scale, interfacial disturbances into large scale, two-fluid coherent structures. The accuracy of the method is comparable to direct calculations of the Navier–Stokes equations. Topology changes in the fluid interface, nonlinear wave interactions, and mean flow distortions are naturally handled in this method, while still retaining the flexibility, computational efficiency, and physical insight of instability-wave based methods. The approach is valid for laminar, convectively unstable, two-fluid shear flows at high Weber numbers, and whose dynamics are dominated by large-scale structures.

1.1. Prior work on linear stability analysis and simulation of two-fluid shear flows

Since the early work of Miles [1,2] on wave generation by wind, a great number of theoretical and computational studies have focused on the initial linear stability mechanism responsible for the growth of two-fluid disturbances. For instance, the investigations of Yih [3], Hooper and Boyd [4], and Renardy and Joseph [5,6], have elucidated several linear mechanisms regarding the formation of interfacial waves and their behavior in various short and long wavelength asymptotic limits. However, because of the assumptions made in linear theory, the results of these studies are generally applicable only during the early stages of the development of instability waves, when the amplitude of the interfacial deformation remains minimal. Nonlinear effects, such as interactions between instability waves, and the distortion of the mean flow due to the disturbances, are typically ignored, despite their importance to the waves' evolution [7].

Attempts to account for some of these effects has resulted in the development of several weakly nonlinear theories. The works of King and McCready [8] and Sangalli et al. [9,10] have considered the effects of finite amplitude waves in two-fluid, bounded channel flows. Similarly, Renardy and Renardy [11] studied the effect of harmonic forcing and derived amplitude equations describing the mean shift mode. These formulations, and others developed in similar vein [12,13], generally lead to Stuart–Landau, Ginzburg–Landau, or Kuramoto–Sivashinsky equations governing the evolution of interfacial disturbances. Despite the improvements due to these models, weakly nonlinear theories remain valid only for marginally unstable frequencies, and cannot model the growth of strongly amplified instabilities. In addition, changes in the interfacial topology were excluded, preventing the theories from fully capturing the development of large scale, two-fluid structures.

As a result of these limitations, current work in modeling the dynamics of high-amplitude instability waves and emerging structures has relied on direct numerical simulations of the Navier–Stokes equations, combined with an appropriate interface tracking scheme. Despite the computational cost, this combination has been used to capture both the nonlinear evolution of flow structures, and also the complicated deformations of the interface. A variety of different interface tracking schemes have been proposed in recent years for use in two-phase simulations, including volume-of-fluid [14], diffuse interface [15,16], and surface marker [17,18] and front tracking [19] methods. Of particular interest to the current work are scalar-based methods, such as the level set method developed by Osher and Sethian [20], Sussman et al. [21] and refined by others [22,23], because of their compatibility with nonlinear instability wave formulations. Many current implementations of the level set method represent the location of the interface by an iso-surface of a smooth function, generally chosen to be the signed distance function, which is evolved forward in time through a passive scalar equation.

Using direct computations with interface tracking, several investigations of two-fluid shear flows have been carried out by Scardovelli and Zaleski [24], Boeck et al. [25], Nourgaliev et al. [26], and Bagué et al. [27]. These studies have focused mainly on the temporal formation of interfacial structures in a small periodic domain. This choice circumvents the demanding computational requirements associated with spatial calculations. As the interface becomes increasingly distorted, and phenomena such as pinch-off and droplet formation appear, more sophisticated mesh refinement techniques [28–30] are required and add additional complexity to the calculations. For these reasons, high-fidelity simulations of realistic, *spatially developing* two-fluid mixing layers, boundary layers, and jets still remain relatively rare. Overcoming these limitations, both in computation and stability theory, motivates our work in seeking an alternative formulation.

1.2. Formulating a nonlinear instability wave method with interface capturing

The nonlinear stability method presented here has its mathematical foundation in the original work of Bertolotti et al. [31] and Herbert [32]. Their studies of boundary layer transition using the nonlinear PSE (NPSE) showed how nonparallel, nonlinear, and finite-amplitude effects could be incorporated into a parabolic system which could be efficiently solved by streamwise marching. Since these initial investigations, additional studies have applied the PSE to problems in receptivity [33], combustion [34], and aeroacoustics [35]. These previous studies have conclusively shown that the NPSE can accurately capture the dynamics of large scale vortical structures in single-phase mixing layers and jets [36].

The extension of the NPSE approach to handle two-fluid shear layers was first addressed by Cheung and Zaki [7]. Their work demonstrated the importance of accounting for nonlinear interactions and the mean-flow distortion when examining the development of interfacial disturbance waves. However, their approach used a coordinate transformation to track the displacement of the interface. The coordinate mapping required that the interface deformation remained single-valued, and thus precluded the modeling of complex features such as Kelvin–Helmholtz rolls and liquid filaments.

To overcome this limitation, we herein present a nonlinear PSE formulation that incorporates a scalar-based interface capturing scheme, which can accommodate changes to the interfacial topology. Although several different interface tracking methods are mentioned in Section 1.1, not all are compatible with the proposed PSE approach. For instance, diffuse interface methods are highly elliptic, while a surface marker methods are difficult to integrate into the frequency-domain formulation of instability waves. The scalar-based interface capturing scheme, similar to the level-set method, uses a passive scalar to mark the location of the two fluids. Information regarding the interfacial location and curvature can then be determined from the dynamics of the passive scalar. In this particular work, nonlinear perturbations to the scalar marker are considered along with the nonlinear dynamics of the two-fluid flow. In this manner, coherent, two-fluid interfacial structures such as liquid ligaments and rolls can still be represented using the scalar-based interface capturing parabolized stability equations (IC-PSE).

While the earlier study of Cheung and Zaki [7] also used the PSE method to capture interfacial deformations, the current work includes capabilities which were not possible in the previous study. Since the earlier approach relies on a coordinate transformation to track the position of the interface, it is limited to flows where the interface remains single-valued. However, the new formulation captures multiple-valued interfacial deformations and the formation of complex fluid structures using the aforementioned scalar-based interface tracking scheme. The relationship between the two approaches is akin to the difference between using boundary-fitted coordinates and a level-set based method in direct calculations of two-phase flow.

As demonstrated in this work, the method is best suited for flows where the large scale structures are dominant, and small scale, surface tension dominated phenomena are negligible. This allows the method to analyze many high Weber flows of interest, such as the processes which lead to fiber-type atomization in liquid jets, and the initial formation of fluid ligaments in sheared flows.

The discussion of our work proceeds according to the following outline: In Section 2, we present the mathematical formulation of the IC-PSE approach, followed by a description of the numerical methods in Section 3. Comparisons between the IC-PSE formulation and high-fidelity direct Navier–Stokes computations for two-fluid mixing layers are discussed in Section 4. The results from mixing layers exhibiting both vortex roll-up and ligament formation are presented. Finally, in Section 5, we provide a summary and conclusion of our work.

2. Governing equations

In the current work we investigate the dynamics of a spatially developing, laminar, incompressible shear flow composed of two immiscible fluids, and which is forced by instability waves at the inlet of the domain. Although this formulation is capable of handling any convectively unstable, slowly evolving flow, we illustrate the method using a two-fluid mixing layer, similar to the one shown in Fig. 1. For this mixing layer configuration, the free-stream velocities of the upper and lower fluids are U_1 and U_2, respectively. The upper and lower fluids also have densities ρ_1 and ρ_2, and viscosities μ_1 and μ_2. The governing equations for such a system are the Navier–Stokes equations

$$\nabla \cdot \mathbf{u} = 0, \tag{1a}$$

$$\rho\left(\frac{\partial \mathbf{u}}{\partial t} + (\mathbf{u}\cdot\nabla)\mathbf{u}\right) = -\nabla P + \nabla\cdot\left(\mu\left(\nabla\mathbf{u} + \nabla^T\mathbf{u}\right)\right) + \mathbf{T}_\sigma\delta(\mathbf{x}-\mathbf{x}_\mathbf{f}) \tag{1b}$$

for the fluid velocity $\mathbf{u}$, density ρ, pressure P, dynamic viscosity μ, and the surface tension force $\mathbf{T}_\sigma$ acting at the interface location $\mathbf{x}_f$ through the Dirac delta function $\delta(\xi)$. To track the motion of the interface we use the scalar function $g(\mathbf{x},t)$. The scalar function is defined such that $g = 0$ at the interface, $g > 0$ in fluid 1, and $g < 0$ in fluid 2. The evolution of g is determined by the equation

$$\frac{\partial g}{\partial t} + (\mathbf{u}\cdot\nabla)g = 0. \tag{1c}$$

The surface tension force $\mathbf{T}_\sigma$ can be expressed as

$$\mathbf{T}_\sigma = \sigma\kappa\hat{\mathbf{n}},$$

Fig. 1. Schematic of a two-fluid, incompressible mixing layer.

where σ is the surface tension coefficient and κ is the interfacial curvature. The normal vector $\hat{\mathbf{n}}$ to the interface can be expressed in terms of the scalar function g,

$$\hat{\mathbf{n}} = \nabla g/|\nabla g|,$$

yielding the following expression for the interfacial curvature:

$$\kappa = \nabla \cdot \left(\frac{\nabla g}{|\nabla g|}\right).$$

Using the Heaviside function $H(x)$, we can also express the instantaneous density and viscosity fields as

$$\rho(\mathbf{x}, t) = \rho_2 + \Delta\rho H(g(\mathbf{x}, t)), \tag{2}$$
$$\mu(\mathbf{x}, t) = \mu_2 + \Delta\mu H(g(\mathbf{x}, t)), \tag{3}$$

where $\Delta\rho = \rho_1 - \rho_2$ and $\Delta\mu = \mu_1 - \mu_2$.

The discontinuous Heaviside function $H(\xi)$ and the Dirac delta function $\delta(\xi)$ appearing in Eqs. (1b), (2) and (3) are replaced with the continuous approximations

$$H^r(\xi) = \begin{cases} 0, & \xi < -s_1/2, \\ \frac{1}{2}\left(1 + \cos\left(\frac{\pi}{s_1}\left(\xi - \frac{s_1}{2}\right)\right)\right), & |\xi| \leqslant s_1/2, \\ 1, & \xi > s_1/2, \end{cases} \tag{4a}$$

$$\delta^r(\xi) = \begin{cases} 0, & |\xi| > s_2/2, \\ \frac{1}{2s_2}\left(1 + \cos\left(\frac{\pi\xi}{s_2}\right)\right), & |\xi| \leqslant s_2/2, \end{cases} \tag{4b}$$

where s_1 and s_2 are parameters which can be used to control the sharpness of the interface. Typical values of s_1 and s_2 used in this work are given in Section 3.2.

Eqs. (1) can be nondimensionalized using the upper free stream values ρ_1, μ_1, U_1, and a characteristic length scale of the flow problem. In the case of the mixing layer, we choose to use the initial vorticity thickness δ_ω. This results in a nondimensional Reynolds number $\mathrm{Re} = \rho_1 U_1 \delta_\omega/\mu_1$, a 'global' Weber number $\mathrm{We} = \rho_1 U_1^2 \delta_\omega/\sigma$, and the lower stream fluid properties are given by the ratios $\rho_r = \rho_2/\rho_1$ and $\mu_r = \mu_2/\mu_1$. The corresponding nondimensional equations are

$$\nabla \cdot \mathbf{u} = 0, \tag{5a}$$
$$\rho\left(\frac{\partial \mathbf{u}}{\partial t} + (\mathbf{u}\cdot\nabla)\mathbf{u}\right) = -\nabla P + \frac{1}{\mathrm{Re}}\nabla\cdot\left(\mu\left(\nabla\mathbf{u} + \nabla^T\mathbf{u}\right)\right) + \frac{\kappa}{\mathrm{We}}\delta(g(\mathbf{x}, t))\frac{\nabla g}{|\nabla g|}, \tag{5b}$$
$$\frac{\partial g}{\partial t} + (\mathbf{u}\cdot\nabla)g = 0. \tag{5c}$$

The solution of Eqs. (5) is separated into two components: a spanwise- and time-independent mean flow component and the perturbation component. If we assume that the vector of flow variables $\phi = [u\ v\ w\ P\ g]^T$, then this decomposition can be expressed as

$$\phi = \bar{\phi}(\mathbf{x}) + \tilde{\phi}(\mathbf{x}, t), \tag{6}$$

where the overbar indicates spanwise- and time-averaging. Therefore, the perturbation component satisfies $\overline{\tilde{\phi}(\mathbf{x}, t)} = 0$. In order to simultaneously evolve the mean flow and the perturbations using the PSE method, a set of parabolic equations must be formulated for both components. In the following sections, we derive such a system of governing equations for the mean $\bar{\phi}$ and perturbation $\tilde{\phi}$ components, and describe the method by which the two solution components are coupled.

2.1. Mean flow equations

The governing equations for the mean flow components $\bar{\phi} = [\overline{U}\ \overline{V}\ \overline{W}\ \overline{P}\ \overline{G}]$ can be derived by applying a time-average and spanwise-average to Eqs. (5). Without loss of generality, we can simplify the mean flow equations, by assuming that no spanwise mean flow exists, i.e., $\overline{W} = 0$, and that spanwise averaging eliminates any dependence on z, so that $\bar{\phi} = \bar{\phi}(x, y)$. In addition, the mean flow equations can be made parabolic by applying the boundary layer assumptions [37]. For slowly evolving mean flows where the changes in the streamwise direction are much smaller compared to the cross-stream variations, the boundary layer assumptions lead to a faithful approximation of the mean flow at high Reynolds numbers. The final form of the mean flow equations is then given by

$$\frac{\partial \overline{U}}{\partial x}+\frac{\partial \overline{V}}{\partial y}=0, \tag{7a}$$

$$\bar{\rho}\overline{U}\frac{\partial \overline{U}}{\partial x}+\bar{\rho}\overline{V}\frac{\partial \overline{U}}{\partial y}-\frac{\bar{\mu}}{\mathrm{Re}}\frac{\partial^2 \overline{U}}{\partial y^2}-\frac{1}{\mathrm{Re}}\frac{\partial \bar{\mu}}{\partial y}\frac{\partial \overline{U}}{\partial y}=\overline{F}_{mom}, \tag{7b}$$

$$\overline{U}\frac{\partial \overline{G}}{\partial x}+\overline{V}\frac{\partial \overline{G}}{\partial y}=\overline{F}_g. \tag{7c}$$

In Eqs. (7) we have made use of the averaged fluid properties:

$$\bar{\rho}=\rho_2+\Delta\rho\,\overline{H(g(\mathbf{x},t))},\qquad \bar{\mu}=\mu_2+\Delta\mu\,\overline{H(g(\mathbf{x},t))}. \tag{8}$$

Note that the behavior of the averaged term $\overline{H(g)}$ dictates the variation of $\bar{\rho}$ and $\bar{\mu}$ across the interface. Fluctuations in $g(\mathbf{x},t)$ resulting from the oscillation of the interface will result in intermediate values of $\bar{\rho}$ between ρ_1 and ρ_2, and correspondingly for $\bar{\mu}$. This smooths the discontinuities in the mean density and viscosity profiles. However, one should note that the *instantaneous* density and viscosity fields remain sharply defined according to Eqs. (2) and (3), and the difference between the instantaneous and the mean fields is accounted for in the perturbation equations.

Applying nonlinear forcing to the right hand side of Eqs. (7) to compute the distorted mean flow differs from previous NPSE studies [34,36]. In the current work, the distortion is directly incorporated into the mean flow equations, while previous methods, e.g. Day et al. [34], computed it as a zero-frequency instability mode. The forcing terms $\overline{F}_{mom}$ and $\overline{F}_g$ in Eqs. (7) are composed of quadratic and higher order combinations of $\tilde{\phi}$, which can possess a non-zero mean (see Eqs. (10) and (11) in Section 2.2). For instance, the forcing term for the scalar Eq. (7c) is given by $\overline{F}_g=-\overline{\tilde{\mathbf{u}}\cdot\nabla\tilde{g}}$.

It should also be noted that interfacial surface tension does not explicitly appear in the mean flow equations (7). The influence of the surface tension force $\mathbf{T}_\sigma$ on the mean flow primarily occurs through the nonlinear interaction term $\overline{F}_{mom}$, and does not significantly alter the mean flow profile. Previous research [7] demonstrated that the curvature of the mean interface location remains small even in highly nonlinear mixing layer flows, and the effects of surface tension on the mean flow can be safely neglected. Therefore, in the presence of smooth mean density and viscosity fields $\bar{\rho}$ and $\bar{\mu}$, the mean velocities $\overline{\mathbf{U}}$ and their gradients $\partial\overline{\mathbf{U}}/\partial y$ will also be continuous. The role of surface tension in the IC-PSE formulation is discussed in greater detail in Section 2.3.

Eqs. (7) form a parabolic system which can be marched downstream once the appropriate inlet and boundary conditions are provided. However, the mean flow components $\bar{\phi}$ cannot be solved independently of the disturbance components $\tilde{\phi}$ due to the presence of the nonlinear terms $\overline{F}_{mom}$ and $\overline{F}_g$, as well as the influence of $\tilde{g}$ in Eq. (8). The exact nature of this coupling between the mean flow and the disturbance equations is discussed in the following section.

2.2. Disturbance equations

To derive the governing equations for the perturbation variables $\tilde{\phi}$, the decomposition (6) is applied to the Navier–Stokes equations (5). After using (7) to remove all time- and spanwise- independent terms from the system, the resulting equations can be written as

$$\nabla\cdot\tilde{\mathbf{u}}=0, \tag{9a}$$

$$\bar{\rho}\left(\frac{\partial\tilde{\mathbf{u}}}{\partial t}+(\overline{\mathbf{U}}\cdot\nabla)\tilde{\mathbf{u}}+(\tilde{\mathbf{u}}\cdot\nabla)\overline{\mathbf{U}}\right)+\nabla\widetilde{P}-\frac{\bar{\mu}}{\mathrm{Re}}\nabla^2\tilde{\mathbf{u}}=\widetilde{\mathbf{F}}_{mom}, \tag{9b}$$

$$\frac{\partial\tilde{g}}{\partial t}+(\overline{\mathbf{U}}\cdot\nabla)\tilde{g}+(\tilde{\mathbf{u}}\cdot\nabla)\overline{G}=\widetilde{F}_g. \tag{9c}$$

The forcing terms used in the disturbance equations (9) are derived from the complete nonlinear terms given by

$$\begin{aligned}\mathbf{F}_{mom}=&-\bar{\rho}(\tilde{\mathbf{u}}\cdot\nabla)\tilde{\mathbf{u}}+\frac{\kappa}{\mathrm{We}}\delta(g(\mathbf{x},t))\frac{\nabla g}{|\nabla g|}\\&-\tilde{\rho}\left(\frac{\partial\tilde{\mathbf{u}}}{\partial t}+(\overline{\mathbf{U}}\cdot\nabla)\overline{\mathbf{U}}+(\overline{\mathbf{U}}\cdot\nabla)\tilde{\mathbf{u}}+(\tilde{\mathbf{u}}\cdot\nabla)\overline{\mathbf{U}}+(\tilde{\mathbf{u}}\cdot\nabla)\tilde{\mathbf{u}}\right)\\&+\frac{\tilde{\mu}}{\mathrm{Re}}\nabla^2(\overline{\mathbf{U}}+\tilde{\mathbf{u}})+\frac{1}{\mathrm{Re}}\nabla\tilde{\mu}\cdot\left(\nabla\tilde{\mathbf{u}}+\nabla^T\tilde{\mathbf{u}}\right),\end{aligned} \tag{10}$$

$$F_g=-\tilde{\mathbf{u}}\cdot\nabla\tilde{g}. \tag{11}$$

The nonlinear forcing terms $\widetilde{\mathbf{F}}_{mom}$ and $\widetilde{F}_g$ are then found by removing the mean contributions from (10) and (11), such that $\widetilde{\mathbf{F}}_{mom}=\mathbf{F}_{mom}-\overline{\mathbf{F}}_{mom}$ and $\widetilde{F}_g=F_g-\overline{F}_g$. As mentioned in the previous section, the forcing terms for the mean flow equations are also determined through a time- and spanwise-average of (10) and (11). In addition, the fluctuating density and viscosity fields are given by

$$\tilde{\rho}(\mathbf{x},t)=\rho-\bar{\rho}(\mathbf{x}),\quad \tilde{\mu}(\mathbf{x},t)=\mu-\bar{\mu}(\mathbf{x}).$$

Both $\tilde{\rho}$ and $\tilde{\mu}$ are nonlinear functions of $\tilde{\phi}$ due to the Heaviside function acting on g in the definitions (2) and (3).

2.2.1. Instability-wave representation

By representing the perturbation components $\tilde{\phi}$ in terms of instability waves, previous work has shown that the perturbation equations (9) can be further manipulated to yield a parabolized system. This is possible for convectively unstable, slowly evolving flows where upstream propagation is limited. This category of flows includes the mixing layers described in Section 2, as well as convectively unstable boundary layers, jets, and wakes flows [38].

The fundamental observation which permits the equations to be parabolized is that the length scale λ of the instability wave is much smaller than the distance L over which the mean flow varies. This ratio is assumed to be small, such that $\lambda/L \sim \mathrm{Re}^{-1} \ll 1$. In deriving the parabolized stability equations, Bertolotti et al. [31] then assumed that the growth rates and shape (but not overall amplitude) of the instability waves also changed slowly in the downstream direction. This representation for the perturbation variables $\tilde{\phi}$ can be expressed using the modal expansion

$$\tilde{\phi}(x,y,z,t) = \sum_{m,n}^{M,N} \hat{\phi}_{mn}(x,y)\mathcal{A}_{mn}(x)\exp\{i\beta_n z - i\omega_m t\}, \tag{12}$$

where the amplitude factor $\mathcal{A}_{mn}(x)$ is written as

$$\mathcal{A}_{mn}(x) = \epsilon_{mn}\exp\left\{i\int_0^x \alpha_{mn}(\xi)\,\mathrm{d}\xi\right\}. \tag{13}$$

Each shape function $\hat{\phi}_{mn}$ is associated with an initial amplitude ϵ_{mn}, streamwise wavenumber α_{mn}, spanwise wavenumber β_n, and temporal frequency ω_m. Both β_n and ω_m are assumed to be integer multiples of the fundamental wavenumber β_0 and frequency ω_m, such that $\beta_n = n\beta_0$ and $\omega_m = m\omega_0$. In contrast to the modal expansion used in traditional parallel flow linear stability theory, note that both the shape functions $\hat{\phi}_{mn}$ and the wavenumbers α_{mn} are allowed to vary in the streamwise coordinate x. However, because these streamwise variations occur on a much longer spatial scale than the instability wavelength, we can assume that

$$\frac{\partial^2}{\partial x^2}\hat{\phi}_{mn}(x,y) \ll 1, \quad \text{and} \quad \frac{\partial^2}{\partial x^2}\alpha_{mn}(x) \ll 1, \tag{14}$$

and these second order derivatives can be neglected. The rate of evolution of the mean flow is also assumed to be slow, so that

$$\frac{1}{\mathrm{Re}}\frac{\partial\bar{\phi}}{\partial x} \ll 1, \quad \text{and} \quad \frac{\partial^2\bar{\phi}}{\partial x^2} \ll 1 \tag{15}$$

and these terms are also ignored in the analysis. These assumptions can be verified in the calculations *a posteriori*, and in simulations of two-fluid mixing layers, both $\partial^2\hat{\phi}/\partial x^2$ and $\partial^2\alpha/\partial x^2$ were typically found to be $\mathcal{O}(10^{-2})$.

However, it must be noted that the second order derivatives of the disturbances in *physical* space still exist, as the approximation in (14) only applies to quantities in the frequency domain. In general, the p^{th} derivative of $\tilde{\phi}(x,y)$ can be expressed as

$$\frac{\partial^p\tilde{\phi}}{\partial x^p} = \sum_{m,n} i^p\left[(\alpha_{mn})^p\hat{\phi}_{mn} - ip(\alpha_{mn})^{p-1}\frac{\partial\hat{\phi}_{mn}}{\partial x} - i\frac{p(p-1)}{2}(\alpha_{mn})^{p-2}\frac{\partial\alpha_{mn}}{\partial x}\hat{\phi}_{mn}\right]\mathcal{A}_{mn}e^{-i\omega_m t + i\beta_n z}.$$

Inserting the expansion (12) in Eqs. (9), and making use of the approximations in (14) and (15) leads to the final form of the scalar-based interface capturing PSE (IC-PSE):

$$i\alpha_{mn}\hat{u}_{mn} + \frac{\partial\hat{u}_{mn}}{\partial x} + \frac{\partial\hat{v}_{mn}}{\partial y} + i\beta_n\hat{w} = 0, \tag{16a}$$

$$\bar{\rho}\left[-i\omega_m + i\alpha_{mn}\overline{U} + \frac{\partial\overline{U}}{\partial x}\right]\hat{u}_{mn} + \bar{\rho}\overline{V}\frac{\partial\hat{u}_{mn}}{\partial y} + \bar{\rho}\frac{\partial\overline{U}}{\partial y}\hat{v}_{mn} + \frac{\bar{\mu}}{\mathrm{Re}}\left(\alpha_{mn}^2 + \beta_n^2 - \frac{\partial^2}{\partial y^2}\right)\hat{u}_{mn} + \left[\bar{\rho}\overline{U} - 2i\alpha_{mn}\bar{\mu}\right]\frac{\partial\hat{u}_{mn}}{\partial x} + i\alpha_{mn}\hat{p}_{mn} + \frac{\partial\hat{p}_{mn}}{\partial x} - \frac{\bar{\mu}}{\mathrm{Re}}i\frac{\partial\alpha_{mn}}{\partial x}\hat{u}_{mn} = \widehat{\mathcal{F}}_{x,mn}, \tag{16b}$$

$$\bar{\rho}\left[-i\omega_m + i\alpha_{mn}\overline{U} + \frac{\partial\overline{V}}{\partial y}\right]\hat{v}_{mn} + \bar{\rho}\overline{V}\frac{\partial\hat{v}_{mn}}{\partial y} + \bar{\rho}\frac{\partial\overline{V}}{\partial x}\hat{u}_{mn} + \frac{\bar{\mu}}{\mathrm{Re}}\left(\alpha_{mn}^2 + \beta_n^2 - \frac{\partial^2}{\partial y^2}\right)\hat{v}_{mn} + \left[\bar{\rho}\overline{U} - 2i\alpha_{mn}\bar{\mu}\right]\frac{\partial\hat{v}_{mn}}{\partial x} + \frac{\partial\hat{p}_{mn}}{\partial y} - \frac{\bar{\mu}}{\mathrm{Re}}i\frac{\partial\alpha_{mn}}{\partial x}\hat{v}_{mn} = \widehat{\mathcal{F}}_{y,mn}, \tag{16c}$$

$$\bar{\rho}\left[-i\omega_m + i\alpha_{mn}\overline{U}\right]\hat{w}_{mn} + \bar{\rho}\overline{V}\frac{\partial\hat{w}_{mn}}{\partial y} + \frac{\bar{\mu}}{\mathrm{Re}}\left(\alpha_{mn}^2 + \beta_n^2 - \frac{\partial^2}{\partial y^2}\right)\hat{w} + \left[\bar{\mu}\overline{U} - 2i\alpha_{mn}\bar{\mu}\right]\frac{\partial\hat{w}_{mn}}{\partial x} + i\beta_n\hat{p} - \frac{\bar{\mu}}{\mathrm{Re}}i\frac{\partial\alpha_{mn}}{\partial x}\hat{w} = \widehat{\mathcal{F}}_{z,mn}, \tag{16d}$$

$$\left[-i\omega_m + i\alpha_{mn}\overline{U}\right]\hat{g}_{mn} + \overline{V}\frac{\partial\hat{g}_{mn}}{\partial y} + \hat{u}_{mn}\frac{\partial\overline{G}}{\partial x} + \hat{v}_{mn}\frac{\partial\overline{G}}{\partial y} + \overline{U}\frac{\partial\hat{g}}{\partial x} = \widehat{\mathcal{F}}_{g,mn}.$$

Using operator notation, Eqs. (16) can be expressed as

$$\mathcal{L}_{mn}\left\{\hat{\phi}_{mn}\right\} = \widehat{\mathbf{F}}_{mn}/\mathcal{A}_{mn}, \tag{17}$$

where the linear operator $\mathcal{L}_{mn}$ is given by

$$\mathcal{L}_{mn} = -i\omega_m\mathbf{G} + i\alpha_{mn}\mathbf{A} + \mathbf{B}\frac{\partial}{\partial y} + \mathbf{C}\frac{\partial^2}{\partial y^2} + i\beta_n\mathbf{D} + \mathbf{E}_{mn} + \mathbf{M}_{mn}\frac{\partial}{\partial x} + \frac{\partial\alpha_{mn}}{\partial x}\mathbf{N}. \tag{18}$$

The individual matrices **A**, **B**, **C**, **D**, $\mathbf{E}_{mn}$, **G**, $\mathbf{M}_{mn}$, and **N** depend only on the mean flow quantities $\bar{\phi}$, α_{mn}, and β_n, and are given in Appendix A.

However, Eq. (17) alone does not completely specify the solution for the disturbances $\tilde{\phi}$. Because both $\hat{\phi}_{mn}$ and α_{mn} depend on x, streamwise changes in the physical disturbance $\tilde{\phi}$ can be absorbed into either variable. To provide closure to the system and remove this ambiguity in the representation, an additional normalization condition must be applied. In this work, we adopt the integral norm

$$\int_{-\infty}^{\infty}\bar{\rho}\hat{u}^*_{mn}\frac{\partial\hat{u}_{mn}}{\partial x} + \bar{\rho}\,\hat{v}^*_{mn}\frac{\partial\hat{v}_{mn}}{\partial x} + \bar{\rho}\hat{w}^*_{mn}\frac{\partial\hat{w}_{mn}}{\partial x} + \hat{g}_{mn}\frac{\partial\hat{g}_{mn}}{\partial x}\,\mathrm{d}\eta = 0. \tag{19}$$

The norm constrains the growth of the integrated shape function $\int\|\hat{\phi}_{mn}\|^2\,\mathrm{d}y$, such that any exponential growth in the perturbation $\tilde{\phi}$ is absorbed by $\alpha_{mn}(x)$ in the amplitude factor $\mathcal{A}_{mn}(x)$. Although the choice of normalization condition is non-unique, this form of an integral constraint is widely adopted in the literature. A more complete discussion of the normalization condition and the assumptions required in the PSE formulation can be found in Herbert [33].

To ensure that the system remains well-posed, one additional modification to the PSE formulation is necessary. Because upstream propagating characteristics have the potential to destabilize the solution, they must be removed from the system. Following the recommendations of Haj-Hariri [39], the streamwise pressure derivative was modified in the x-momentum equation. This was accomplished by omitting the $\partial\hat{p}/\partial x$ derivative in Eq. (16b), resulting in the following expression for the pressure gradient in physical coordinates:

$$\frac{\partial\tilde{p}}{\partial x} = \sum_{m,n} i\alpha_{mn}\hat{p}_{mn}\mathcal{A}_{mn}(x)e^{i\beta_n z - i\omega_m t}. \tag{20}$$

As mentioned previously, the solution of (17) and (19) is also coupled with the solution of the mean flow equations (7). Therefore, in the downstream marching procedure, both $\hat{\phi}$ and $\bar{\phi}$ are advanced simultaneously in x, and information is exchanged at every step to synchronize the nonlinear terms $\overline{F}_{mom}$, $\overline{F}_g$, and $\hat{\mathcal{F}}_{mn}$. A complete description of the solution procedure is given below in Section 3.

2.2.2. Initial and boundary conditions

The initial conditions for the shape functions $\hat{\phi}_{mn}$ for the IC-PSE system (17) are obtained from the solutions to the parallel flow, linear stability problem. At the inlet position, $x = 0$, the mean flow is assumed to be parallel and a function of y only, such that $\overline{\mathbf{U}} = (\overline{U}(y), 0, 0)$. In the absence of any streamwise dependence, the perturbation equations (9a) and (9b) can be reduced to a single Orr-Sommerfeld differential equation for the velocity eigenfunction $\hat{v}^{OS}(y)$

$$i\mathrm{Re}\frac{\bar{\rho}}{\bar{\mu}}\left[M(\mathrm{D}^2-k^2) - M'' + \frac{\bar{\rho}'}{\bar{\rho}}(M\mathrm{D} - M')\right]\hat{v}^{OS} = \left[(\mathrm{D}^2-k^2) - \frac{\bar{\mu}''}{\bar{\mu}} - 2\frac{\bar{\mu}'}{\bar{\mu}}\mathrm{D}\right](\mathrm{D}^2-k^2)\hat{v}^{OS}, \tag{21}$$

where $k^2 = \alpha^2 + \beta^2$ and $M(y) = \alpha\overline{U}(y) - \omega$, and the differential operator $\mathrm{D} = (\bullet)' = d/dy$. In Eq. (21), the mean density and viscosity are also assumed to be solely functions of y : $\bar{\rho} = \bar{\rho}(y)$ and $\bar{\mu} = \bar{\mu}(y)$.

Malik and Hooper [40] demonstrated that the Orr-Sommerfeld Eq. (21) faithfully captures the stability properties of interfacial flows, provided that the thickness of the interface layer is sufficiently thin. This observation is also noted here, in Fig. 2. For a mixing layer with $\rho_r = 2$, $\mu_r = 1$, the dispersion relation $\alpha(\omega)$ of the miscible interface approaches the two-phase limit as the interface thickness $d \to 0$. At the low frequencies of interest, the growth rate of the miscible interface is relatively insensitive to the thickness d. It should be noted that this discussion is relevant only to the mean density and viscosity profiles. As mentioned previously, the instantaneous, total density and viscosity as given by (2) and (3), remain sharply defined by the Heaviside function.

In the free stream, $y \to \pm\infty$, Eq. (21) reduces to the simpler differential equation

$$i\mathrm{Re}\frac{\bar{\rho}}{\bar{\mu}}\left[M_{1,2}(\mathrm{D}^2-k^2)\right]\hat{v}^{OS} - (\mathrm{D}^2-k^2)^2\hat{v}^{OS} = 0, \quad M_{1,2} = \alpha U_{1,2} - \omega,$$

from which the far-field boundary conditions on $\hat{v}^{OS}(y)$ can be determined. After solving for the velocity eigenfunction in (21), the other eigenfunction components can be found from $\hat{v}^{OS}(y)$, yielding the vector of components $\hat{\phi}^{OS}_{mn} = \left[\hat{u}^{OS}\ \hat{v}^{OS}\ \hat{w}^{OS}\ \hat{p}^{OS}\ \hat{g}^{OS}\right]$ for the disturbances at a particular frequency ω_m and spanwise wavenumber β_n. For instance, the eigenfunction for the scalar component can be written as

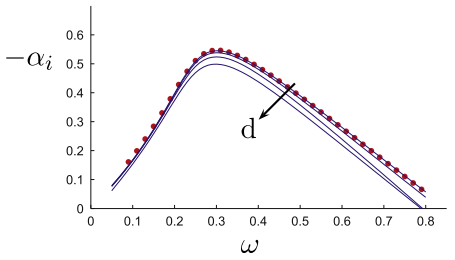

Fig. 2. Effect of the interface width $d = 0.10, 0.25, 0.50, 0.75$ on the dispersion relation $\alpha(\omega)$ for a $\rho_r = 2$, $\mu_r = 1$ mixing layer. The infinitesimally sharp mixing layer is indicated by the dots (•).

$$\hat{g}^{OS}(y) = \frac{-\hat{v}^{OS}(y)\overline{G}'(y)}{iM}.$$

The full physical disturbance used at the inlet of the NPSE system (17) can be constructed as a time dependent superposition of $\hat{\phi}^{OS}_{mn}$:

$$\tilde{\phi}(x = 0, y, z, t) = \sum_{m,n} \epsilon_{mn}\hat{\phi}^{OS}_{mn}(y)e^{-i\omega_m t + i\beta_n z}.$$

All mixing layers studied in this work used harmonic forcing at the inlet, such that the temporal and spanwise frequencies are integer multiples of the fundamental frequencies: $\omega_m = m\omega_0$ and $\beta_n = n\beta_0$. In general, ω_0 and β_0 were chosen to be close to the most unstable mode at the inlet of the two-phase shear flows.

2.3. Surface tension effects

As previously mentioned, the IC-PSE formulation is applicable for flows in which the dynamics of large-scale vortical structures are dominant, and where small scale phenomena can be neglected. Small scale phenomena, such as droplet pinch-off or coalescence, are driven primarily through surface tension forces, and can give rise to absolute instabilities or upstream propagating characteristics. Therefore, the effects of surface tension should be very carefully considered within the currently developed framework, and great care should be taken to ensure that the application of surface tension forces falls within the PSE assumptions. Specifically, two items must be considered: (1) that arbitrarily small Weber numbers are not compatible with the parabolization process, and (2) strong surface tension effects can lead to the growth of absolute instabilities, which are undesirable.

To examine the first point, consider the momentum Eq. (16b), written for a single mode $\hat{\phi} = [\hat{u}\ \hat{v}\ \hat{w}\ \hat{p}\ \hat{g}]$ prior to the application of the PSE assumptions (14) and (15):

$$\bar{\rho}\left[\left(-i\omega + i\alpha\overline{U} + \frac{\partial\overline{U}}{\partial x}\right)\hat{u} + \overline{U}\frac{\partial\hat{u}}{\partial x} + \overline{V}\frac{\partial\hat{u}}{\partial y} + \frac{\partial\overline{U}}{\partial y}\hat{v}\right] - \frac{\bar{\mu}}{\mathrm{Re}}\left[-(\alpha^2+\beta^2)\hat{u} + \frac{\partial^2\hat{u}}{\partial y^2} + \frac{\partial^2\hat{u}}{\partial x^2} + 2i\alpha\frac{\partial\hat{u}}{\partial x} + i\frac{\partial\alpha}{\partial x}\hat{u}\right] + i\alpha\hat{p} + \frac{\partial\hat{p}}{\partial x} = \widehat{\mathcal{F}}_x.$$

The left hand side of the equation consists of a linear operator acting on shape functions $\hat{\phi}$, while the right hand side $\widehat{F}$ consists of all nonlinear forcing terms, including the surface tension term T_σ. To parabolize the equations, all streamwise second order derivatives must be removed to prevent elliptic effects from appearing. This is achieved by adopting a slowly varying coordinate $X = x/\mathrm{Re}$ and using the following scalings:

$$\partial/\partial x \sim \mathcal{O}(1/\mathrm{Re}), \quad \overline{V} \sim \mathcal{O}(1/\mathrm{Re}).$$

Inserting these scalings into the left hand side of the equation, and eliminating all terms of $\mathcal{O}(\mathrm{Re}^{-3})$ or higher gives

$$\bar{\rho}\left[\left(-i\omega + i\alpha\overline{U} + \frac{1}{\mathrm{Re}}\frac{\partial\overline{U}}{\partial X}\right)\hat{u} + \frac{\overline{U}}{\mathrm{Re}}\frac{\partial\hat{u}}{\partial X} + \frac{\overline{V}}{\mathrm{Re}}\frac{\partial\hat{u}}{\partial y} + \frac{\partial\overline{U}}{\partial y}\hat{v}\right] + \left(i\alpha + \frac{1}{\mathrm{Re}}\frac{\partial}{\partial X}\right)\hat{p}$$
$$-\frac{\bar{\mu}}{\mathrm{Re}}\left(-(\alpha^2+\beta^2)\hat{u} + \frac{2i\alpha}{\mathrm{Re}}\frac{\partial\hat{u}}{\partial X} + \frac{i}{\mathrm{Re}}\frac{\partial\alpha}{\partial X} + \frac{\partial\hat{u}}{\partial y^2}\right) = \widehat{\mathcal{F}}_x$$

Note that the left hand side operator is now parabolic, as the second order derivative $\partial^2/\partial x^2$ is of order $\mathcal{O}(\mathrm{Re}^{-3})$ and has been neglected. A similar analysis must be performed on the right hand side to eliminate any ellipticity of the nonlinear terms. In particular, we focus on the nondimensional surface tension term $\mathbf{T}_{\boldsymbol{\sigma}} = \kappa\hat{\mathbf{n}}/\mathrm{We}$, which contains ellipticity due to the curvature κ, defined as

$$\kappa = \nabla\cdot\left(\frac{\nabla g}{|\nabla g|}\right) = \frac{1}{\sqrt{h}}\frac{\partial^2 g}{\partial x_i\partial x_i} - \frac{1}{h^{3/2}}\frac{\partial^2 g}{\partial x_i\partial x_j}\frac{\partial g}{\partial x_i}\frac{\partial g}{\partial x_j},$$

where

$$h = |\nabla g|^2 = \frac{\partial g}{\partial x_i}\frac{\partial g}{\partial x_i}.$$

Using the modal representation of the scalar $g(x,y,t)$ in the definition of κ, and inserting it into the surface tension force gives

$$T_{\sigma,x} = \frac{1}{\mathrm{We}}\left[\frac{1}{\sqrt{h}}\left(\frac{\partial^2 \hat{g}}{\partial x^2} + 2i\alpha\frac{\partial \hat{g}}{\partial x} + \left(i\frac{\partial \hat{g}}{\partial x} + \alpha^2\right)\hat{g} + \frac{\partial \hat{g}}{\partial y^2}\right) - \cdots\right]\hat{\mathbf{n}}\cdot\hat{\mathbf{e}}_x.$$

Applying the same slowly varying coordinate as above, we find that the first term in the above expression scales as $\frac{1}{\sqrt{h}}\frac{1}{\mathrm{We}}\frac{1}{\mathrm{Re}^2}\frac{\partial^2 \hat{g}}{\partial X^2}$. In order to eliminate this second order derivative, we require that it be of $\mathcal{O}(\mathrm{Re}^{-3})$, the same order as the viscous term above. This leads to the conclusion that

$$\mathrm{We}^{-1} \sim \mathcal{O}(\mathrm{Re}^{-1}).$$

Thus, in order for the equations to be successfully parabolized, surface tension forces should not dominate viscous forces in the flow, or the ratio $\mathrm{Re}/\mathrm{We} \lesssim 1$. This scaling supplements the original assumptions regarding the PSE, which states that the spread of the mean flow occurs on the order $\mathrm{Re}^{-1} \ll 1$. Additionally, it should be noted that the global Weber number We (based on the vorticity thickness δ_ω) should be sufficiently large so that the local Weber number (based on the characteristic ligament thickness) also remains high, and local surface tension forces remain negligible. This is discussed in further detail below.

The second point regarding surface tension concerns the generation of absolute instabilities, which have significant implications in the context of PSE simulations. The previous work of Leib and Goldstein [41,42] showed that, at sufficiently strong surface tension ($\mathrm{We} \sim \mathcal{O}(1)$), the capillary instability of a liquid jet transitions from a convective to an absolute instability. Similar observations were made for the effect of surface tension in planar liquid jets by Rees and Juniper [43]. These absolute instabilities are characterized by the spatial growth of disturbances in the upstream and downstream direction, as well as temporal growth at any fixed location. In the current case, however, the PSE formulation only describes downstream convective instabilities. Careful consideration must be applied to eliminate the appearance of absolute instabilities from all sources, including capillary effects and countercurrent flows, since the parabolization process alone does not guarantee the well-posedness of the formulation. Despite the lack of absolute instabilities, convective instabilities remain essential in the study of primary break-up in liquid jets and sheets. The work of Lin and Reitz [44] has shown that convective instabilities are the root cause of jet break-up through a variety of mechanisms, such as Rayleigh or wind-induced instabilities, and atomization processes.

The primary atomization of liquid jets, even with weak surface tension, underscores the importance of examining large scale structures in interfacial dynamics. Marmottant and Villermaux [45] and Lasheras and Hopfinger [46] have shown that, at high Weber numbers, the creation of fine ligaments can eventually lead to fiber-type atomization in a liquid jet. Because the size of the liquid ligaments and fibers are likely determined by vortical structures near the interface, accurate IC-PSE models for the liquid structures can be valuable to the study of jet break-up.

3. Numerical method

The numerical solution to the mean flow equations (7), the IC-PSE system (17), and the normalization condition (19) is found using an iterative downstream marching procedure. This ensures that the mean flow $\bar{\phi}$, disturbance components $\tilde{\phi}$, and the normalization condition all converge to a consistent solution at each streamwise position. The following section discusses the discretization and solution methods for each component of the solution, and an overview of the solution procedure is outlined in Section 3.3.

3.1. Mean flow

The mean flow boundary layer equations (7) are discretized using a semi-implicit Crank–Nicolson scheme, similar to that discussed in Fletcher [47]. Given the mean flow solution $\bar{\phi}^k = \left[\overline{U}^k\ \overline{V}^k\ 0\ 0\ \overline{G}^k\right]$ and mean profiles $\bar{\rho}^k,\ \bar{\mu}^k$ at the position x^k, then the solution $\bar{\phi}^{k+1}$ at the next position x^{k+1} can be found by inverting the following system:

$$\frac{1}{\Delta x}\left[\bar{\rho}\overline{U}\right]^k\overline{U}^{k+1} - \frac{1}{2}H_X\left\{\overline{U}^{k+1}\right\} = \frac{1}{\Delta x}\left[\bar{\rho}\overline{U}\right]^k\overline{U}^k + \frac{1}{2}H_X\left\{\overline{U}^k\right\} + \frac{1}{2}\left\{\overline{F}^{k+1} + \overline{F}^k\right\}, \tag{22a}$$

$$\mathrm{D}_1\left\{\overline{V}^{k+1}\right\} = -\frac{1}{\Delta x}\left[\overline{U}^{k+1} - \overline{U}^k\right], \tag{22b}$$

$$\frac{1}{\Delta x}\overline{U}^k\overline{G}^{k+1} - \frac{1}{2}H_G\left\{\overline{G}^{k+1}\right\} = \frac{1}{\Delta x}\overline{U}^k\overline{G}^k + \frac{1}{2}H_G\left\{\overline{G}^k\right\}. \tag{22c}$$

As mentioned previously, the mean flow is assumed to be two-dimensional ($\overline{W} = 0$), and the mean pressure is assumed to be constant, which we set $\overline{P} = 0$ for convenience here. The H_X and H_G operators are composed of the convective and viscous components

$$H_X\left\{\overline{U}^{k'}\right\} = -\bar{\rho}^k\overline{V}^k \mathrm{D}_1\left\{\overline{U}^{k'}\right\} + \frac{\mathrm{D}_1\left\{\bar{\mu}^k\right\}}{\mathrm{Re}}\mathrm{D}_1\left\{\overline{U}^{k'}\right\} + \frac{\bar{\mu}^k}{\mathrm{Re}}\mathrm{D}_2\left\{\overline{U}^{k'}\right\},$$
$$H_G\left\{\overline{G}^{k'}\right\} = -\bar{\rho}^k\overline{V}^k \mathrm{D}_1\left\{\overline{G}^{k'}\right\}.$$

The D_1 and D_2 operators correspond to the fourth order central difference operators in the cross-stream direction:

$$\mathrm{D}_1\left\{A_l^k\right\} = \frac{A_{l-2}^k - 8A_{l-1}^k + 8A_{l+1}^k - A_{l+2}^k}{12\Delta y}, \tag{23a}$$
$$\mathrm{D}_2\left\{A_l^k\right\} = \frac{-A_{l-2}^k + 16A_{l-1}^k - 30A_l^k + 16A_{l+1}^k - A_{l+2}^k}{12(\Delta y)^2}, \tag{23b}$$

where $A_l^k = A(x^k, y^l)$. The upper and lower boundary conditions on the streamwise velocity are given by

$$\overline{U}(y=\infty) = U_1, \quad \overline{U}(y=-\infty) = U_2.$$

The initial mean flow profile used in the calculation is determined from the similarity solution $\overline{U}^{SS}(y)$ of the laminar two-fluid mixing layer (see Section 4-4.1 from [37]), such that $\overline{U}(x^k=0,y) = \overline{U}^{SS}(y)$. The similarity solution also provides the boundary conditions for the vertical velocity, so that $\overline{V}(y=\pm\infty) = \overline{V}^{SS}_{\pm\infty}$.

The scalar function $g(\mathbf{x},t)$ used in this method also carries a different interpretation when compared to previous approaches, in particular the level-set method. Due to its decomposition into mean and perturbation components, and the instability wave representation of $\tilde{g}(\mathbf{x},t)$, the scalar function used here cannot be interpreted as a signed distance function. In order to be compatible with the normalization condition (19), the perturbation component $\tilde{g}(\mathbf{x},t)$ should vanish at infinity and remain square-integrable. For this to occur, we require that the mean gradient $\partial\overline{G}/\partial y$ also vanish in the free stream, but adopt a constant value in the sheared region of the flow. These conditions can be satisfied by specifying

$$\frac{\partial\overline{G}}{\partial y} = \frac{s_g}{4}\left(1 - \tanh\left(\frac{y-y_+}{s_w}\right)\right)\left(1 + \tanh\left(\frac{y-y_-}{s_w}\right)\right)$$

at the inlet, which can be integrated to give the initial scalar profile

$$\overline{G}(y) = \frac{s_w s_g}{4}\left\{-\log\left(\cosh\left(\frac{y-y_+}{s_w}\right)\right) + \log\left(\cosh\left(\frac{y-y_-}{s_w}\right)\right) + \coth\left(\frac{y_+-y_-}{s_w}\right)\left[\log\left(\cosh\left(\frac{y-y_-}{s_w}\right)\right) - \log\left(\cosh\left(\frac{y-y_-}{s_w}\right)\right)\right]\right.$$

The parameters $y_\pm$ determine the locations where $\overline{G}(y)$ transitions from a linear slope to a zero slope function, and s_w and s_g determine the transition width and the values of the slope, respectively. In the simulations of two-phase mixing layers shown in Section 4, the numerical parameters were typically $s_w = 0.25$, $s_g = 0.50$, and $y_\pm = \pm 2.0$. An example of an initial scalar profile $\overline{G}(y)$ is shown in Fig. 3.

3.2. Disturbance equations

The numerical discretization of the combined NPSE and scalar-based interface capturing equations (17)–(19) follows established procedures. The work of Andersson et al. [48] has demonstrated that marching the PSE system using an explicit scheme led to instability problems, while Herbert [32] showed that second-order implicit schemes did not out-perform lower-order schemes. Therefore, the first order implicit scheme described below is similar to the method used by Day et al. [34], Cheung and Lele [36], and Cheung and Zaki [7].

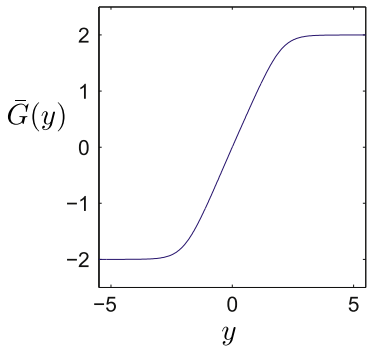

Fig. 3. The initial profile $\overline{G}(y)$.

For the sake of compactness, the PSE operator (18) can be regrouped into the following form:

$$\mathcal{L}_{mn} = \mathbf{L}_{mn} + \mathbf{M}_{mn}\frac{\partial}{\partial x} + \mathbf{N}\frac{\partial \alpha_{mn}}{\partial x}$$

The cross-stream derivatives $\partial/\partial y$ and $\partial^2/\partial y^2$ in $\mathbf{L}_{mn}$ are evaluated using the fourth order difference scheme (23). The discontinuous Heaviside function $H(\xi)$ and the Dirac delta function $\delta(\xi)$ are replaced with the continuous approximations (4a) and (4b), where s_1 and s_2 were typically chosen to be $s_1 = 0.125$ and $s_2 = 0.125$ at the inlet. The use of the regularized $H^r(\xi)$ and $\delta^r(x)$ ensures that the shape functions $\hat{\phi}_{mn}$ remain continuous and the y-derivatives can be evaluated throughout the entire domain.

In addition, the streamwise derivative $\partial/\partial x$ is evaluated using first order implicit differentiation

$$\left.\frac{\partial \hat{\phi}}{\partial x}\right|_{k+1} = \frac{\hat{\phi}^{k+1} - \hat{\phi}^{k}}{\Delta x}, \quad \left.\frac{\partial \alpha}{\partial x}\right|_{k+1} = \frac{\alpha^{k+1} - \alpha^{k}}{\Delta x},$$

resulting in the discretized form of Eq. (17)

$$\left[(\Delta x)\mathbf{L}_{mn}^{k+1} + \mathbf{M}_{mn}^{k+1} + (\alpha_{mn}^{k+1} - \alpha_{mn}^{k})\mathbf{N}^{k+1}\right]\hat{\phi}_{mn}^{k+1} = \mathbf{M}_{mn}^{k+1}\hat{\phi}_{mn}^{k} + \frac{\widehat{\mathbf{F}}_{mn}^{k+1}}{\mathcal{A}_{mn}^{k+1}}\Delta x \tag{24}$$

for the shape function $\hat{\phi}_{mn}^{k+1}$ at position x^{k+1}. In order for $\hat{\phi}$ to also satisfy the normalization condition at each streamwise position, an iterative process is used. At each iteration level j, Eq. (24) is solved for $\hat{\phi}_{mn}^{k+1\,j}$ given a guess of the wave number $\alpha_{mn}^{k+1\,j}$ and the α_{mn}^{k}, $\hat{\phi}_{mn}^{k}$ from the previous streamwise position x^k. The guess for the wave number at the next iteration level $j+1$ is determined using an iterative version of the normalization condition (19)

$$\alpha_{mn}^{k+1\,j+1} = \alpha_{mn}^{k+1\,j} - \frac{i}{\Delta x}\frac{\int \bar{\rho}\left(\hat{\mathbf{u}}_{mn}^{k+1\,j}\right)^{*}\cdot\Delta\hat{\mathbf{u}}_{mn}^{k+1\,j} + \left(\hat{g}_{mn}^{k+1\,j}\right)^{*}\cdot\Delta\hat{g}_{mn}^{k+1\,j}\,\mathrm{d}\eta}{\int \bar{\rho}\left|\hat{\mathbf{u}}_{mn}^{k+1\,j}\right|^{2} + \left|\hat{g}_{mn}^{k+1\,j}\right|^{2}\mathrm{d}\eta}, \tag{25}$$

where $\Delta\hat{\mathbf{u}}_{mn}^{k+1\,j} = \hat{\mathbf{u}}_{mn}^{k+1\,j} - \hat{\mathbf{u}}_{mn}^{k\,j}$ and $\Delta\hat{g}_{mn}^{k+1\,j} = \hat{g}_{mn}^{k+1\,j} - \hat{g}_{mn}^{k\,j}$. Thus, at each position x^{k+1}, Eqs. (24) and (25) are solved repeatedly until the fractional change in α_{mn} reaches a specified tolerance:

$$\left|\alpha_{mn}^{k+1\,j+1} - \alpha_{mn}^{k+1\,j}\right| / \left|\alpha_{mn}^{k+1\,j+1}\right| < \varepsilon_{TOL}. \tag{26}$$

Due to the coupling between the mean flow and the disturbance components, changes to $\hat{\phi}_{mn}$ during this iteration process can also lead to changes in $\bar{\phi}$. To maintain consistency between the two components, the mean flow equations (7) must also be re-evaluated at every iteration level to obtain the appropriate $\bar{\phi}^{k+1\,j}$ for use in Eq. (24). This method of calculating the mean flow distortion differs from the conventional approach, e.g. Day et al. [34]. The current approach is more robust than using the zero frequency mode. An outline of the complete iteration process and the solution procedure is given in Section 3.3.

3.2.1. Nonlinear terms

When a larger number of modes are used in the representation (12), an explicit representation of the nonlinear terms in the frequency domain becomes algebraically unfeasible. Instead, the nonlinear terms are evaluated in physical space. Subsequently, using the relationship

$$\widetilde{\mathbf{F}}(\mathbf{x},t) = \sum_{m,n}\widehat{\mathbf{F}}_{mn}(x,y)e^{-i\omega_m t + i\beta_n z}, \tag{27}$$

the forcing terms $\widehat{\mathbf{F}}_{mn}$ in Eq. (17) are found through a Fast Fourier Transform (FFT). Aliasing errors were avoided in the computation of the FFT by adhering to the 3/2 zero-padding rule in both directions.

The nonlinear terms for the mean flow equations (7) can also be determined through (27). More precisely, the zero-frequency terms represent the time-averaged and spanwise-averaged component of $\mathbf{F}(\mathbf{x},t)$. It should be noted that the inclusion of the highly nonlinear surface tension term $\mathbf{T}_{\boldsymbol{\sigma}}$ to the forcing $\mathbf{F}(\mathbf{x},t)$ can present convergence difficulties to the scalar based IC-PSE solution procedure. Surface tension forces due to curvature of the interface can be elliptic in nature, which can interfere with the parabolization assumptions mentioned earlier. In addition, previous work by Rees and Juniper [43] has indicated that surface tension can cause the shear layer to transition from convectively unstable to absolutely unstable, even in the presence of co-flow. To avoid these difficulties, this investigation focuses on two-fluid mixing layers with relatively weak surface tension, and where the Weber number is of the same order, or larger, than the Reynolds number.

3.2.2. Grid stretching

Because interfacial deformations are generally limited to regions of higher velocity shear, a non-uniform grid allows for the efficient allocation of computational grid points. A non-uniform grid is used in both the x and y directions, for instance, the sinh mapping

$$y(\zeta) = \frac{L_y}{2}\frac{\sinh(b_y\zeta)}{\sinh(b_y)}$$

is used to map the uniformly distributed coordinate $-1 \leqslant \zeta \leqslant 1$ to the physical $-L_y/2 \leqslant y \leqslant L_y/2$ grid. Typical mixing layer simulations shown in Section 4 used a domain length of $L_y = 12.0$ and a stretch factor $b_y = 3.0$. Similar stretching was adopted in the streamwise direction, where the computational domain is divided into several regions, each with a different Δx (see Fig. 4). This allows the combined IC-PSE method to capture the downstream formation of large scale structures in higher resolution. However, it should be noted that arbitrarily small step-sizes cannot be used for highly nonlinear, subsonic flows, since a minimum Δx is required to avoid destabilization of the PSE due to residual ellipticity [49].

It is also important to note that the stepsize Δx does not limit the x-resolution of features in physical space. Instead, restrictions on Δx govern how fast changes in the shape function $\hat{\phi}_{mn}(x,y)$ and the wavenumber $\alpha_{mn}(x,y)$ can be accommodated. Generally speaking, increased physical resolution of the fluctuations $\tilde{\phi}(x,y)$ can be achieved by including a greater number of modal harmonics $\hat{\phi}_{mn}$ in the simulation.

3.3. PSE solution procedure

The general algorithm for solving the combined IC-PSE problem can be summarized using the following pseudocode:

for $k = 1, N_x - 1$ **do**
  while modes not converged **do**
    Update nonlinear terms **F** (Eqs. (10) and (11))
    Solve for new mean flow $\bar{\phi}^{k+1}$ (Eq. (7))
    for each mode (m,n) **do**
      Solve for $\hat{\phi}_{mn}^{k+1}$ (Eq. (24))
      Update α_{mn}^{k+1} (Eq. (25))
    end for
  end while
end for

At every streamwise position, the shape functions $\hat{\phi}_{mn}^{k+1}$ and wavenumbers α_{mn}^{k+1} are repeatedly solved for, until they satisfy the convergence criteria (26). The nonlinear terms **F** and mean flow $\bar{\phi}^{k+1}$ must also be updated with each new solution, in order to maintain consistency between the mean flow and disturbance components.

Memory storage requirements are kept low because the streamwise marching procedure requires information only from the k and $k+1$ streamwise positions (due to the implicit Euler differentiation scheme). The computational work for solving the IC-PSE also scales nearly linearly with the number of the modes used in the simulation. This is possible because the computational time required to compute the nonlinear terms **F** is small compared to the solution of the main PSE system (24). The solution procedure was parallelized using the MPI framework, by assigning each processor to solve for a different $\hat{\phi}_{mn}$ shape function. At each iteration step, the designated master processor computes the updated mean flow $\bar{\phi}^{k+1}$ and nonlinear terms **F**, and distributes them to the appropriate processors.

4. Validation

Initial validation of the IC-PSE formulation was conducted through comparisons with the two-fluid PSE method of Cheung and Zaki [7]. In that work, a coordinate transformation was used to track the growth of the two-fluid interface. This allowed

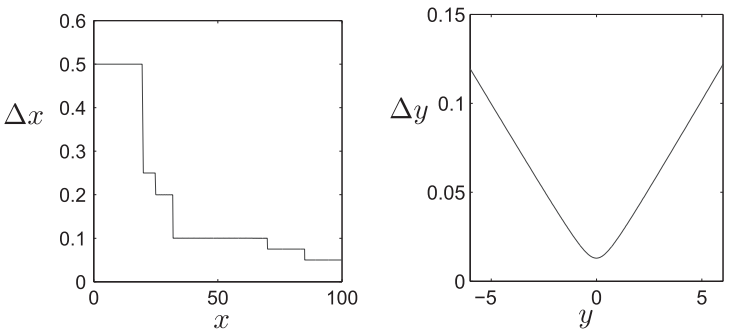

Fig. 4. The grid stretching in x and y directions.

for finite interfacial deformation, but was restricted to single-valid interfacial topologies. Comparisons between the methods, as seen in Fig. 5, show close agreement in the growth and behavior of the instability waves.

However, it should be noted that such comparisons are valid only when the interfacial deformations remain single valued, and before the appearance of wave crests or other complex topological features. Extending these comparisons downstream would be inappropriate, as the capabilities of the two formulations are quite different. Validating the IC-PSE formulation in these regions requires comparisons against direct calculations, as discussed in the remainder of this section.

4.1. Direct calculations

The scalar-based IC-PSE methodology is further validated against direct two-phase calculations of the Navier–Stokes equations. The governing equations (1) are solved using a fractional step method with a conservative level set scheme [50,23]. The computational algorithm makes use of a staggered grid with a local volume flux formulation in curvilinear coordinates [51,52]. Adams-Bashforth scheme is implemented for the explicit time advancement of convective terms. Pressure and diffusion terms are treated by implicit Euler method, and by Crank–Nicolson method, respectively. This code is parallelized using Message Passing Interface (MPI).

A level-set approach was chosen for interface tracking in the direct calculations. Advantages of such a choice include automatic handling of topological changes, efficient parallelization, as well as easy representation of the interface curvature. As mentioned in the introduction, the conventional level-set technique relies on representing the interface as the zero level set of a signed distance function. However, one of the main limitations of this method is poor mass conservation. The present study exploits the conservative level-set method in conjunction with a ghost fluid approach [23]. The conservative level set method ensures the accurate and robust interface transport by using a hyperbolic tangent level set function. Moreover, the sharp discontinuity of the interface can be captured by the ghost fluid method.

A series of comparisons between the IC-PSE and direct calculations are discussed in the following sections. Initial tests of the IC-PSE method have shown this approach to be viable for density and viscosity ratios of up to at least ρ_r, $\mu_r \sim \mathcal{O}(10)$. The comparisons presented here are at moderate density and viscosity ratios for the following reasons: At higher ratios, the direct calculations require an order of magnitude larger computational cost in order to resolve the fine-scale features generated by the higher frequency harmonics, due to the smaller spatial wavelengths involved. In addition, the behavior of the instability waves in the direct computations becomes sensitive to the treatment of viscosity in the interface capturing scheme [25]. Finally, larger density and viscosity ratios lead to rapid growth and saturation of the eigenmodes, before the appearance of large-scale structures and is therefore not ideally suited for the validation of the IC-PSE capabilities. Therefore, for the purpose of validation, the lower density and viscosity ratios were selected, such that well-identified flow structures emerged and the corresponding direct simulations could be completed with reasonable computational costs.

Comparisons between the IC-PSE and the direct calculations are presented for mixing layers with density and viscosity ratios $\rho_r = 2$, $\mu_r = 5$, $U_2/U_1 = 0.5$. In Section 4.2, this mixing layer is computed with a higher Reynolds number (Re = 250) to validate the IC-PSE code for shear layers where vortex roll-up and large-scale vortical structures dominate. Section 4.3 discusses a lower Reynolds number case (Re = 100), where the behavior of the nonlinear instability waves leads to the appearance of liquid fingers and ligaments. The final example in Section 4.4 shows the computation of a three-dimensional mixing layer using the IC-PSE method.

4.2. Mixing layer simulation with roll-up

The first comparison between the IC-PSE and the direct Navier–Stokes computations is discussed for a two-dimensional, $\rho_r = 2$, $\mu_r = 5$, $U_2/U_1 = 0.5$ mixing layer with Reynolds number Re = 250, and without the effects of surface tension (We = ∞).

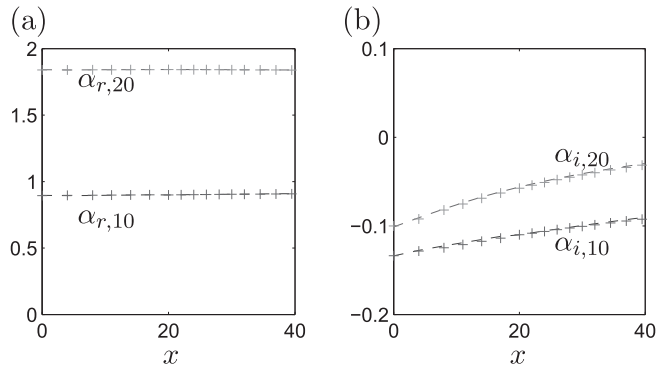

Fig. 5. Comparison between the IC-PSE (dashed lines – –) and the PSE with coordinate transformation (crosses +) for a mixing layer with $U_2/U_1 = 0.5$, $\rho_2/\rho_1 = 2$, $\mu_2/\mu_1 = 1$, Re = 350. The streamwise wavenumbers $\alpha_r(x)$ are shown in (a), while the growth rates $\alpha_i(x)$ are shown in (b) for both the fundamental and first harmonic.

The IC-PSE simulations used a total of 8 modes ($M = 8$, $N = 0$) in the two-dimensional calculations, where the frequency spectra, and initial inlet amplitudes for each of the modes are given in Table 1. It should be noted that computational studies with different numbers of harmonics indicated that the results remained unchanged for values of $M \geqslant 8$. The computational domain was $L_x \times L_y = 100\delta_0 \times 12\delta_0$ in size, and the direct Navier–Stokes calculations used 2049×257 ($N_x \times N_y$) grid points, while the IC-PSE used 976×301 ($N_x \times N_y$) grid points. The time required to complete the calculation on a distributed memory Intel Xeon cluster was approximately 925 CPU-hours for the Navier–Stokes computation (800 CPU-hours to remove the transients , and 125 CPU-hours to gather statistics), versus approximately 40 CPU-hours for the IC-PSE computation.

A qualitative comparison between the two different computations is shown in Fig. 6. In both the direct Navier–Stokes computations and the IC-PSE simulations, the growth of the instability waves leads to the appearance of large scale vortical structures. Vortex roll-up is observed to occur at the same locations in both simulations, and the strength of the vortical structures is also similar (Fig. 6(b)). Using the nonlinear stability method, the calculated interface behavior also shows excellent agreement with the direct Navier–Stokes computations. In Fig. 6(a), we can see that the position at which the interfacial wave crests and forms vortex rolls is well captured using this method. By comparison, linear and weakly nonlinear theories would be valid only up to $x \approx 20$, and the work of Cheung and Zaki [7] would only capture the interfacial deformation up to the point of cresting ($x \approx 40$).

An overlay of the two interface locations (at analogous instants in time) provides a closer comparison between the two calculations. In Fig. 7, the size and shape of the vortex rolls are shown to agree remarkably well. The entrainment of the fluid ligaments into the vortex rolls is well captured by the IC-PSE method, with the only visible differences are the earlier predictions of droplet formation when compared to the direct Navier–Stokes calculations.

A quantitative comparison of the growth of large-scale structures can be obtained by examining the instantaneous density thickness, defined by

$$\theta_\rho(x,t) \equiv \int_{-\infty}^{\infty} \frac{\rho(x,y,t) - \rho_{ref}(y)}{\rho_2 - \rho_1} \mathrm{d}y,$$

where ρ_{ref} is the nominal inlet density profile $\rho_{ref}(y) = \rho_2 + \Delta\rho H(y)$. This quantity measures the departure of the local density profile at any instant (x,t) from its initial state ρ_{ref}. Large values of θ_ρ indicate the degree of penetration of one immiscible fluid into the other. In Fig. 8, the streamwise variation of θ_ρ is computed using the results from both the IC-PSE and the direct calculations. Excellent agreement between the two methods can be observed, even as the mixing layer forms complex vortex rolls downstream.

Additional comparisons of the mean quantities can be made by examining time-averaged profiles of the flow variables. In Fig. 9(a)–(c), the mean density profiles $\bar{\rho}(y)$ from both the direct Navier–Stokes and the IC-PSE computations are shown at three different streamwise positions $x = \{40, 65, 100\}$, which correspond to points before, near, and after the first vortex roll-up location. At all three streamwise positions, the density profiles from the direct Navier–Stokes computations and the IC-PSE show relatively good agreement, even in the sheared region where large scale, coherent structures dominate the dynamics of the mixing layer.

The expansion of the mixing layer due to the formation of large-scale vortical structures is also well captured by the IC-PSE method. In Fig. 9(d), the streamwise development of mean momentum thickness is plotted, using the following definition for $\theta_{mom}(x)$

$$\theta_{mom}(x) \equiv \int \left(\frac{\overline{U}(y) - U_2}{U_1 - U_2}\right)\left(1 - \frac{\overline{U}(y) - U_2}{U_1 - U_2}\right) \mathrm{d}y$$

Although the initial behavior of the two-phase mixing layers is similar to the unperturbed case, both the IC-PSE and the direct computations show a rapid expansion of the mixing layer near the vortex roll-up location. This expansion has been previously noted by Ho and Huerre [53], who attribute the sudden growth to nonlinear interactions between the fundamental mode and its higher harmonics. The ability of the IC-PSE method to account for this behavior is heavily dependent on correctly capturing the mean flow corrections (Section 2.1).

The IC-PSE method is also able to correctly predict the nonlinear behavior of individual modes. A comparison of the integrated modal energy from both the direct and IC-PSE calculations is shown in Fig. 10, using the following kinetic energy definition:

$$E_{mn}(x) = \int_{-\infty}^{\infty} \bar{\rho}\left(|\hat{u}'_{mn}|^2 + |\hat{v}'_{mn}|^2 + |\hat{w}'_{mn}|^2\right) \mathrm{d}y,$$

Table 1
Initial parameters for the mixing layer with $\rho_r = 2$, $\mu_r = 5$, $U_2/U_1 = 0.5$, Re = 250, We = ∞.

m	ω	ϵ_{mn}
1	0.40	2.5×10^{-3}
2	0.80	5×10^{-5}
$\geqslant 3$	$m \times 0.40$	10^{-5}

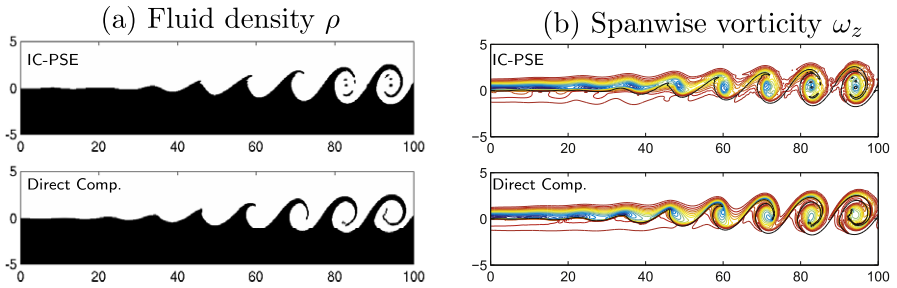

Fig. 6. A comparison of the instantaneous (a) fluid density ρ and (b) spanwise vorticity ω_z for the $\rho_r = 2$, $\mu_r = 5$, $U_2/U_1 = 0.5$, Re = 250, We = ∞ mixing layer for the direct and IC-PSE computations. The density levels range from 1 to 2, and vorticity contours range from -0.5 to -0.05 in steps of 0.025.

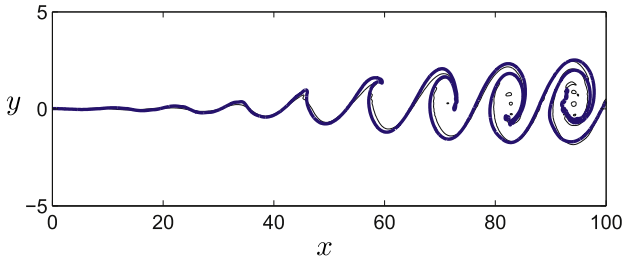

Fig. 7. Comparison of the instantaneous fluid interface between direct (thick solid line ▬) and IC-PSE (thin solid line —) computations of the mixing layer in Fig. 6.

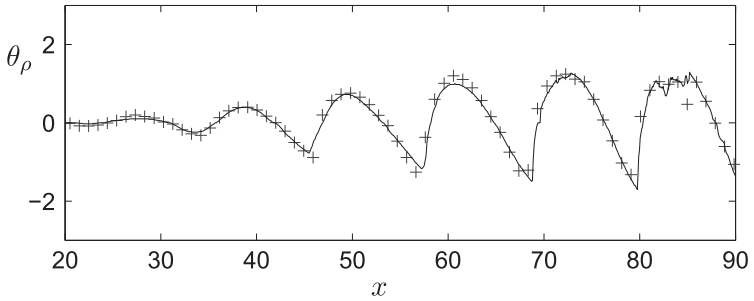

Fig. 8. The density thickness θ_ρ for the mixing layer in Fig. 6, with the direct calculation shown in crosses (+), and IC-PSE shown in solid lines (—).

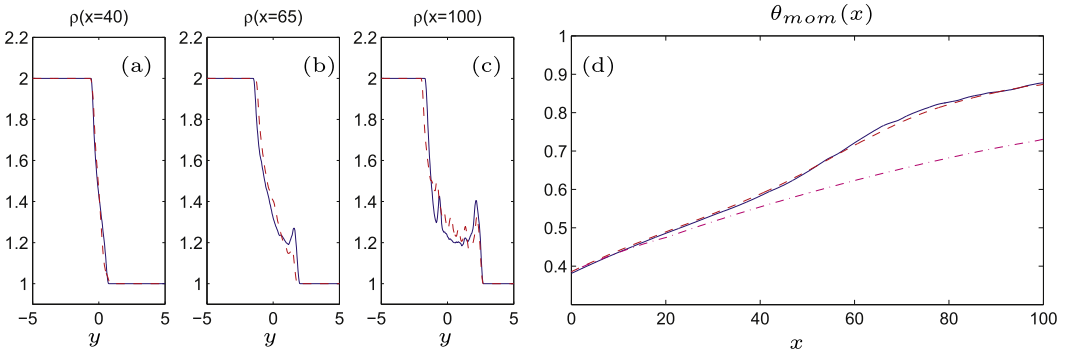

Fig. 9. (a)–(c): The mean density profiles $\bar{\rho}(y)$ at locations $x = 40$, 65, and 100, and (d) momentum thickness $\theta_{mom}(x)$ for the direct computation, (Solid line —), IC-PSE (dashed line – –), and the unperturbed mean flow (dash-dot line – · –).

where $\hat{\phi}'_{mn} = \hat{\phi}_{mn}(x,y)\mathcal{A}_{mn}(x)$. Both approaches yield the same results at the two lowest frequencies, the fundamental mode (E_{10}) and the first harmonic (E_{20}) mode. The streamwise behavior of these instability waves follows a similar pattern: an

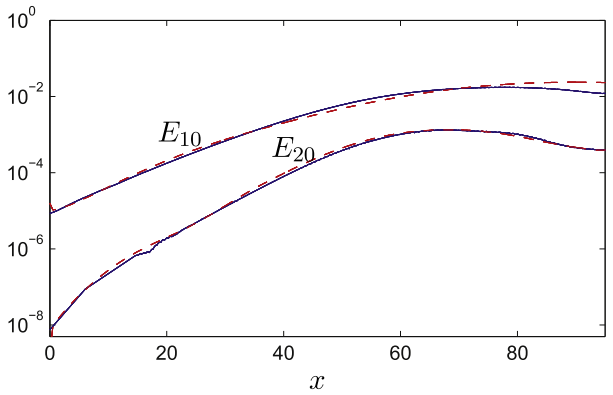

Fig. 10. Modal energy E_{mn} for the direct (Solid line —) and IC-PSE (dashed line – –) computations of the $\rho_r = 2$, $\mu_r = 5$, $U_2/U_1 = 0.5$, Re = 250, We = ∞ mixing layer.

initial, linear region where the growth is exponential, followed by a nonlinear region where the modes saturate and slowly decay. Both the IC-PSE and direct computations predict identical saturation locations and amplitudes for the two modes, suggesting that the nonlinear interactions between instability waves have been properly captured by the scalar-based IC-PSE method.

4.3. Mixing layer simulation with ligament formation

A second comparison between the IC-PSE and direct Navier–Stokes computations was performed in order to examine the formation of liquid ligaments in mixing layers where roll-up does not occur. As suggested by Boeck [25], at lower Reynolds numbers, the more rapid expansion of the mixing layer decreases the strength of the vorticity and inhibits roll-up. The resulting ligaments which evolve from interfacial disturbances are not entrained into Kelvin cat's-eye patterns, and any liquid drops which break off have a higher probability of being carried into the upper stream.

The parameters for the second mixing layer comparison are similar to the those in Section 4.2, except for the effects of fluid inertia and surface tension. The density, viscosity, and velocity ratios remained unchanged ($\rho_r = 2$, $\mu_r = 5$, $U_2/U_1 = 0.5$), but the Reynolds number has been decreased to Re = 100 and a finite Weber number We = 2500 is used. A longer streamwise domain was used, with grid sizes ($N_x \times N_y$) of 4097×257 for the direct computations, and 1188×451 for the equivalent IC-PSE. The initial conditions for the $M = 8$ modes used in the IC-PSE are given in Table 2. The total computational time required for each simulation on an Intel Xeon cluster was approximately 3400 CPU-hours for the direct computations (3000 CPU-hours to compute two flow-through times, and 400 CPU-hours to gather statistics), and approximately 64 CPU-hours for the IC-PSE.

As shown in Fig. 11, the increased momentum diffusion in the mixing layer inhibits the growth of instability waves and the subsequent formation of large scale, vortical structures. When compared to the equivalent picture in Fig. 6(b), we can see that the weaker vorticity concentrations are insufficient to cause vortex roll-up, although liquid ligaments are seen to lift up into the upper stream. A side-by-side comparison of the IC-PSE and direct computations in Fig. 11(a) demonstrates that both methods predict similar wave growth and ligament formation, to the same degree accuracy shown in Section 4.2. This is also seen in the comparison of the instantaneous fluid interface positions in Fig. 12, and the instantaneous density thickness θ_ρ in Fig. 13. Both calculations show that the growth of the large scale structures and ligaments in the mixing layer are halted before any roll-up process can occur. The formation of these ligaments is qualitatively similar to the nonlinear computations of sheared fluid interfaces performed by Boeck et al. [25] and Tauber et al. [54].

The mean flow statistics derived from this mixing layer also show excellent agreement between the IC-PSE and the direct computations. The evolution of the mixing layer is well-captured by the nonlinear instability wave method, as illustrated by the mean density $\bar{\rho}$ profiles and the momentum thickness $\theta_{mom}(x)$ plots in Fig. 14. When compared to previous mixing layer

Table 2
Initial parameters for the mixing layer with $\rho_r = 2$, $\mu_r = 5$, $U_2/U_1 = 0.5$, Re = 100, and We = 2500.

m	ω	ϵ_{mn}
1	0.35	1×10^{-3}
2	0.70	1×10^{-4}
3	1.05	1×10^{-5}
$\geqslant 4$	$m \times 0.35$	10^{-6}

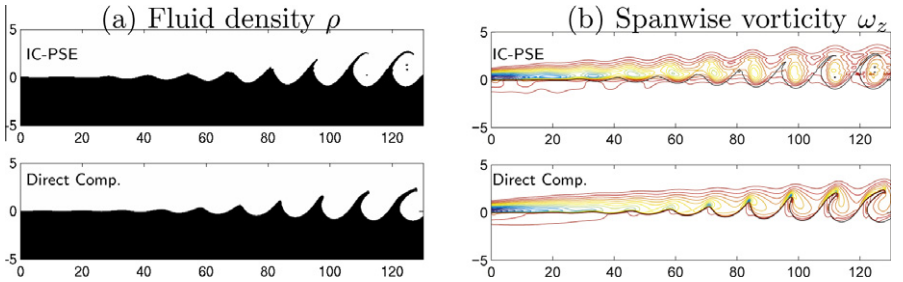

Fig. 11. A comparison of the instantaneous (a) fluid location ρ and (b) spanwise vorticity ω_z for the $\rho_r = 2$, $\mu_r = 5$, $U_2/U_1 = 0.5$, Re = 100, We = 2500 mixing layer for the direct and IC-PSE computations. The density levels range from 1 to 2, and vorticity contours range from -0.5 to -0.05 in steps of 0.025.

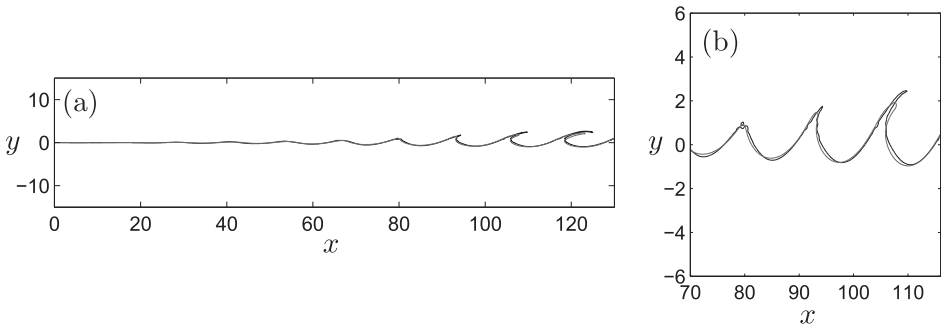

Fig. 12. (a) Comparison of the instantaneous fluid interface between direct (thick solid line ▬) and IC-PSE (thin solid line —) computations of the mixing layer in Fig. 11. (b) Close in view of the region between $70 \leqslant x \leqslant 115$.

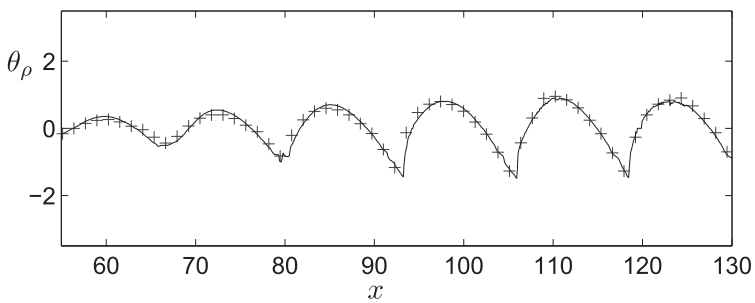

Fig. 13. The density thickness θ_ρ for the mixing layer in Fig. 11, with the direct calculation shown in crosses (+), and IC-PSE shown in solid lines (—).

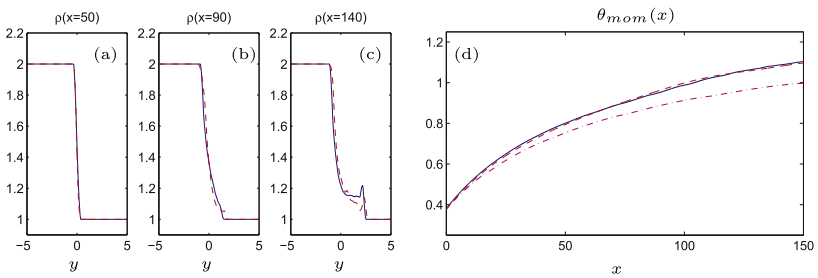

Fig. 14. (a)–(c): The mean density profiles $\bar{\rho}(y)$ at locations $x = 50$, 90, and 140, and (d) momentum thickness $\theta_{mom}(x)$ for the direct computation (solid line —), IC-PSE (dashed line – –), and the unperturbed mean flow (dash-dot line – · –).

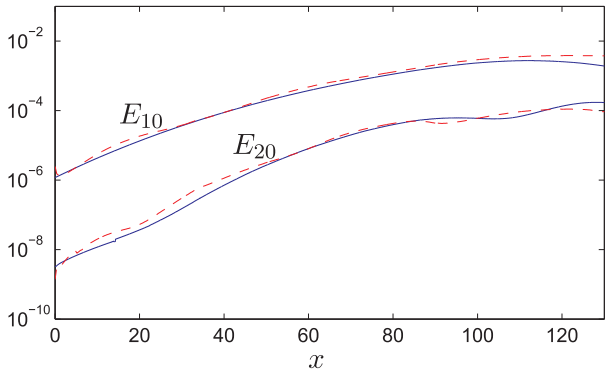

Fig. 15. Modal energy E_{mn} for the direct calculation (Solid line —), IC-PSE (dashed line – –) computations of the $\rho_2/\rho_1 = 2$, $\mu_2/\mu_1 = 5$, $U_2/U_1 = 0.5$, Re = 100, We = 2500 mixing layer.

Table 3
Initial parameters for the three-dimensional mixing layer with $\rho_r = 2$, $\mu_r = 5$, $U_2/U_1 = 0.5$.

m	n	ω	ϵ_{mn}
0	$n > 0$	0.00	1×10^{-4}
1	0	0.35	1×10^{-4}
1	1	0.35	5×10^{-4}
1	2	0.35	1×10^{-4}
1	3	0.35	1×10^{-4}
1	4	0.35	1×10^{-4}
2	$0 \leqslant n \leqslant 4$	0.70	1×10^{-4}
$\geqslant 3$	$0 \leqslant n \leqslant 4$	$m \times 0.35$	1×10^{-6}

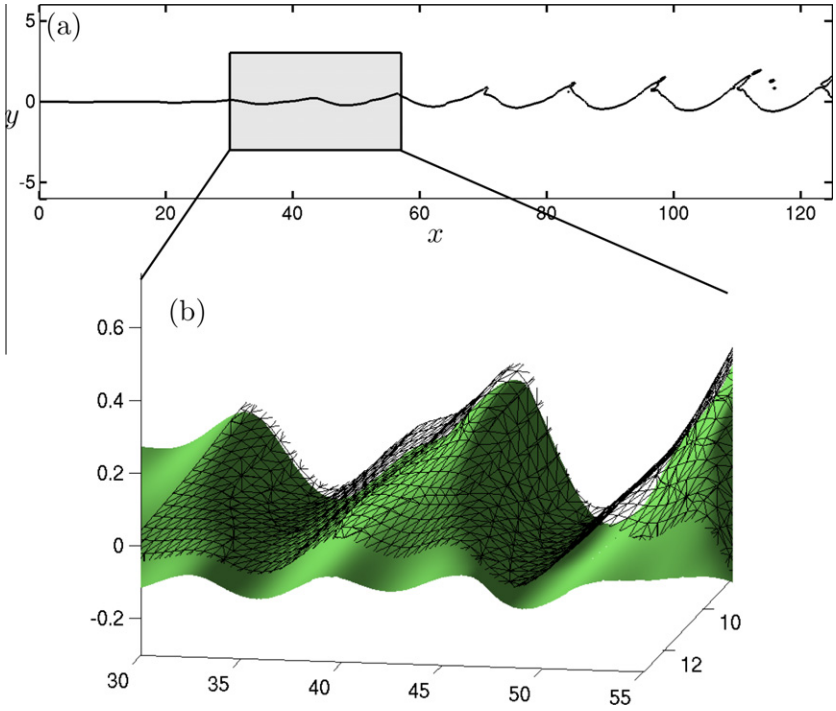

Fig. 16. (a) The instantaneous fluid interface at the plane $z \approx 8$ for the three-dimensional $\rho_r = 2$, $\mu_r = 5$, $U_2/U_1 = 0.5$ mixing layer of Section 4.4, computed using IC-PSE. Shown in the shaded region is the subdomain which was also computed through direct calculations. (b) Three-dimensional comparison of the instantaneous fluid interface. The IC-PSE interface is shown with the solid surface, while the interface from the direct calculation is shown using the wire mesh and offset slightly in the z-direction.

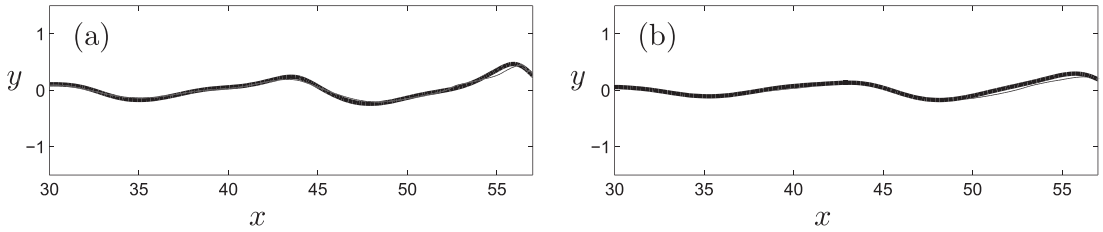

Fig. 17. Cross section of the interfacial location from the mixing layer shown in Fig. 16, taken near (a) $z \approx 8$ and (b) $z \approx 11.5$. The direct calculation is shown in thick solid lines (━━), the IC-PSE in thin solid lines (−−).

in Section 4.2, the spread of the mixing layer is more gradual, and lacks the sudden expansion due to vortex roll-up observed in Fig. 9.

The ability of the IC-PSE method to capture the nonlinear behavior of the interfacial waves is also shown in Fig. 15. The initial growth and eventual saturation of the fundamental (E_{10}) and the first harmonic (E_{20}) energies agree with the energies calculated from direct computations.

4.4. Three-dimensional mixing layer simulation

In the third example of an IC-PSE computation, we consider a three-dimensional version of the mixing layer in Section 4.3. Similar flow parameters are used, with the density, viscosity, and velocity ratios $\rho_r = 2$, $\mu_r = 5$, $U_2/U_1 = 0.5$, respectively. The Reynolds number is Re = 100, the Weber number is We = 10,000, and the base spanwise frequency is set to $\beta = 0.2$. All instability modes up to $(M,N) = (6,4)$ were included in the calculation, and the initial parameters for each of these modes are given in Table 3. Primary forcing at the inlet is through the $(1,1)$ spanwise fundamental. For this problem, the IC-PSE solution required approximately 1000 CPU-hours to compute over a domain of approximately $L_x \times L_y = 150 \times 15$.

The computational requirements for the entire three-dimensional simulation would be demanding for the equivalent Navier–Stokes calculation. Approximately 66 million nodes are required in order to accurately capture the thee-dimensional development of the interface throughout the whole domain. In addition to the grid requirements, the computational cost of the Navier–Stokes calculation is exacerbated by the need to remove initial transients, prior to the collection of statistics.

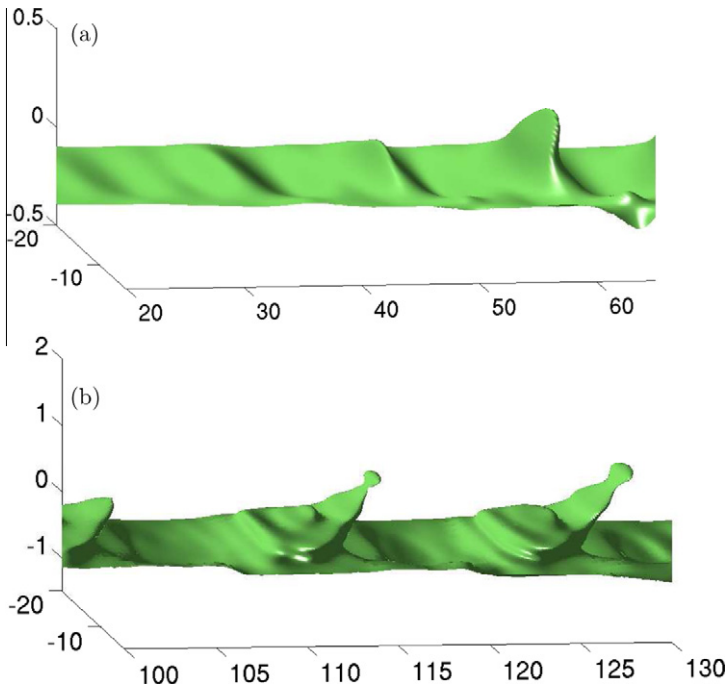

Fig. 18. The instantaneous interfacial location of the three dimensional mixing layer, showing the (a) early wave development, and (b) ligament formation process.

This problem can be simplified by examining direct calculations of the three-dimensional problem over a smaller domain, and then comparing the results to a subdomain of the IC-PSE calculation. Using this strategy, a limited domain of $L_x \times L_y \times L_z = 10\pi \times 12 \times 10\pi$ was chosen for the direct calculation, and computed using 4.3 million grid points. Initial inlet data was taken from the IC-PSE at $x = 30$.

An instantaneous snapshot of the fluid interface during this early development region is shown in Fig. 16, and very good agreement between the wave structures is observed. A cross-section of through the wave through the locations $z \approx 8$ and $z \approx 11.5$, seen in Fig. 17, also shows that the growth of the primary forcing mode and the amplitude of the interfacial wave is relatively well captured.

The growth of large-scale, two fluid structures from the initial formation of these interfacial waves can be seen by examining the entire domain of the IC-PSE calculation. Compared to the two-dimensional mixing layer in Section 4.3, the lower initial forcing amplitude in the three-dimensional case yielded shorter ligaments (see Fig. 16). However, the three-dimensional view of the ligaments displays a more complicated structure. During the initial growth of the interface perturbation, the wave deforms in a sheet-like manner with relatively gentle variations in the spanwise direction (Fig. 18(a)). As the perturbations develop downstream, the crests are lifted up towards the higher speed stream, and are stretched to form ligaments. Eventually the ligaments undergo "necking" as a precursor to break-up and droplet formation (Fig. 18(b)). These results are in qualitative agreement with previous computations discussed in Scardovelli and Zaleski [24], as well as the experiments of Marmottant and Villermaux [45] on breakup in liquid jets.

5. Conclusions

In this work, we have presented an accurate and efficient methodology for computing the growth of interfacial stability waves in spatially developing, two-fluid flows. The formulation combines the nonlinear parabolized stability equations with a scalar-based interface capturing scheme. Therefore, the method can capture finite amplitude, interacting instability waves, and can accommodate changes in the interfacial topology. As demonstrated in this study, the new method allows two-fluid stability methods to handle more realistic flows with large scale, two-fluid structures and complicated interfacial evolution.

Computations using both the IC-PSE method and direct calculations of the Navier–Stokes equations were performed for two-fluid mixing layers with density ratio $\rho_r = 2$ and viscosity ratio $\mu_r = 5$. A comparison of results indicated that the IC-PSE method was able to accurately capture the formation of large scale structures, such as rolls or ligaments, inside the mixing layer very accurately. The growth and evolution of the instability waves, in addition to the distortions to the mean flow were well predicted by the IC-PSE method. Three-dimensional simulations also showed that this method is capable of capturing the structure and evolution of ligaments. With regards to computational costs, the IC-PSE calculations is at least an order of magnitude more efficient than the direct solutions of the Navier–Stokes equations.

Ongoing work on the IC-PSE formulation is devoted towards applying the method to other flow configurations. At higher density and viscosity ratios, the behavior of the interfacial instability waves may be sensitive to the treatment of the viscosity in the interface capturing scheme. In order to accurately simulate the dynamics of low capillary number flows, such as air/water systems, the effects of surface tension must also be incorporated into the fine-scale features which develop downstream.

Acknowledgments

This research was supported by a Marie Curie International Incoming Fellowship within the 7th European Community Framework Programme. Further support was provided by the UK Engineering and Physical Sciences Research Council (EPSRC). The authors also wish to thank Dr. Seo Yoon Jung for performing the direct computations which were used for validation.

Appendix A

Given the vector of flow variables $\hat{\phi} = [\hat{u}\ \hat{v}\ \hat{w}\ \hat{p}\ \hat{g}]^T$ and the linear operator in Eq. (18),

$$\mathcal{L}_{mn} = -i\omega_m \mathbf{G} + i\alpha_{mn}\mathbf{A} + \mathbf{B}\frac{\partial}{\partial y} + \mathbf{C}\frac{\partial^2}{\partial y^2} + i\beta_n \mathbf{D} + \mathbf{E}_{mn} + \mathbf{M}_{mn}\frac{\partial}{\partial x} + \frac{\partial \alpha_{mn}}{\partial x}\mathbf{N}.$$

the individual matrices **A**, **B**, **C**, **D**, $\mathbf{E}_{mn}$, **G**, $\mathbf{M}_{mn}$, and **N** can be expressed as

$$\mathbf{A} = \begin{pmatrix} \bar{\rho}\overline{U} & 0 & 0 & 1 & 0 \\ 0 & \bar{\rho}\overline{U} & 0 & 0 & 0 \\ 0 & 0 & \bar{\rho}\overline{U} & 0 & 0 \\ 1 & 0 & 0 & 0 & 0 \\ 0 & 0 & 0 & 0 & \overline{U} \end{pmatrix} \quad \mathbf{B} = \begin{pmatrix} \bar{\rho}\overline{V} & 0 & 0 & 0 & 0 \\ 0 & \bar{\rho}\overline{V} & 0 & 1 & 0 \\ 0 & 0 & \bar{\rho}\overline{V} & 0 & 0 \\ 0 & 1 & 0 & 0 & 0 \\ 0 & 0 & 0 & 0 & \overline{V} \end{pmatrix},$$

$$\mathbf{C} = -\frac{\bar{\mu}}{\mathrm{Re}}\begin{pmatrix} 1 & 0 & 0 & 0 & 0 \\ 0 & 1 & 0 & 0 & 0 \\ 0 & 0 & 1 & 0 & 0 \\ 0 & 0 & 0 & 0 & 0 \\ 0 & 0 & 0 & 0 & 0 \end{pmatrix},$$

$$\mathbf{E}_{mn} = \begin{pmatrix} \bar{\rho}\frac{\partial \overline{U}}{\partial x} + \frac{\bar{\mu}}{\mathrm{Re}}\gamma_{mn}^2 & \bar{\rho}\frac{\partial \overline{U}}{\partial y} & \bar{\rho}\frac{\partial \overline{U}}{\partial z} & 0 & 0 \\ \bar{\rho}\frac{\partial \overline{V}}{\partial x} & \bar{\rho}\frac{\partial \overline{V}}{\partial y} + \frac{\mu}{\mathrm{Re}}\gamma_{mn}^2 & \bar{\rho}\frac{\partial \overline{V}}{\partial z} & 0 & 0 \\ \bar{\rho}\frac{\partial \overline{W}}{\partial x} & \bar{\rho}\frac{\partial \overline{W}}{\partial y} & \bar{\rho}\frac{\partial \overline{W}}{\partial \eta} + \frac{\bar{\mu}}{\mathrm{Re}}\gamma_{mn}^2 & 0 & 0 \\ 0 & 0 & 0 & 0 & 0 \\ \frac{\partial \overline{G}}{\partial x} & \frac{\partial \overline{G}}{\partial y} & \frac{\partial \overline{G}}{\partial z} & 0 & 0 \end{pmatrix},$$

$$\mathbf{D} = \begin{pmatrix} \bar{\rho}\overline{W} & 0 & 0 & 0 & 0 \\ 0 & \bar{\rho}\overline{W} & 0 & 0 & 0 \\ 0 & 0 & \bar{\rho}\overline{W} & 1 & 0 \\ 0 & 0 & 1 & 0 & 0 \\ 0 & 0 & 0 & 0 & \overline{W} \end{pmatrix} \quad \mathbf{G} = \begin{pmatrix} \bar{\rho} & 0 & 0 & 0 & 0 \\ 0 & \bar{\rho} & 0 & 0 & 0 \\ 0 & 0 & \bar{\rho} & 0 & 0 \\ 0 & 0 & 0 & 0 & 0 \\ 0 & 0 & 0 & 0 & 1 \end{pmatrix},$$

$$\mathbf{M}_{mn} = \begin{pmatrix} \bar{\rho}\overline{U} - 2i\alpha_{mn}\frac{\bar{\mu}}{\mathrm{Re}} & 0 & 0 & 0 & 0 \\ 0 & \rho\overline{U} - 2i\alpha_{mn}\frac{\bar{\mu}}{\mathrm{Re}} & 0 & 0 & 0 \\ 0 & 0 & \rho\overline{U} - 2i\alpha_{mn}\frac{\bar{\mu}}{\mathrm{Re}} & 0 & 0 \\ 1 & 0 & 0 & 0 & 0 \\ 0 & 0 & 0 & 0 & \overline{U} \end{pmatrix},$$

$$\mathbf{N} = -\frac{i\bar{\mu}}{\mathrm{Re}}\begin{pmatrix} 1 & 0 & 0 & 0 & 0 \\ 0 & 1 & 0 & 0 & 0 \\ 0 & 0 & 1 & 0 & 0 \\ 0 & 0 & 0 & 0 & 0 \\ 0 & 0 & 0 & 0 & 0 \end{pmatrix}.$$

In matrix $\mathbf{E}_{mn}$, $\gamma_{mn}^2 = \alpha_{mn}^2 + \beta_n^2$. For the purposes of this work, the matrices have been simplified by neglecting the spanwise mean flow, i.e., $\overline{W} = 0$, and by assuming that the mean flow is independent of the spanwise coordinate, i.e., $\bar{\phi} = \bar{\phi}(x, y)$ only.

References

[1] J.W. Miles, On the generation of surface waves by shear flows, Journal of Fluid Mechanics 3 (1957) 185–204.
[2] J.W. Miles, The hydrodynamic stability of a thin film of liquid in uniform shearing motion, Journal of Fluid Mechanics 8 (1960) 593–610.
[3] C.S. Yih, Instability due to viscosity stratification, Journal of Fluid Mechanics 27 (1967) 337–352.
[4] A.P. Hooper, W.G.C. Boyd, Shear-flow instability at the interface between two viscous fluids, Journal of Fluid Mechanics 128 (1983) 507–528.
[5] Y. Renardy, D.D. Joseph, Couette flow of two fluids between concentric cylinders, Journal of Fluid Mechanics 150 (1985) 381–394.
[6] Y. Renardy, D.D. Joseph, Oscillatory instability in a Bénard problem of two fluids, Physics of Fluids 28 (1985) 788–793.
[7] L.C. Cheung, T.A. Zaki, Linear and nonlinear instability waves in spatially developing two-phase mixing layers, Physics of Fluids 22 (2010) 052103.
[8] M.R. King, M.J. McCready, Weakly nonlinear simulation of planar stratified flows, Physics of Fluids 12 (2000) 92–102.
[9] M. Sangalli, C.T. Gallagher, D.T. Leighton, H.-C. Chang, M.J. McCready, Finite-amplitude waves at the interface between fluids with different viscosity: theory and experiments, Physical Review Letters 75 (1995) 77–80.
[10] M. Sangalli, M.J. McCready, H.-C. Chang, Stabilization mechanisms of short waves in stratified gas–liquid flow, Physics of Fluids 9 (1997) 919–939.
[11] M. Renardy, Y. Renardy, Derivation of amplitude equations and analysis of sideband instabilities in two-layer flows, Physics of Fluids A: Fluid Dynamics 5 (1993) 2738–2762.
[12] A.P. Hooper, R. Grimshaw, Nonlinear instability at the interface between two viscous fluids, Physics of Fluids 28 (1985) 37–45.
[13] Y. Renardy, Weakly nonlinear behavior of periodic disturbances in two-layer Couette–Poiseuille flow, Physics of Fluids A: Fluid Dynamics 1 (1989) 1666–1676.
[14] D. Gueyffier, J. Li, A. Nadim, R. Scardovelli, S. Zaleski, Volume-of-fluid interface tracking with smoothed surface stress methods for three-dimensional flows, Journal of Computational Physics 152 (1999) 423–456.
[15] D.M. Anderson, G.B. McFadden, A.A. Wheeler, Diffuse-interface methods in fluid mechanics, Annual Review of Fluid Mechanics 30 (1998) 139–165.
[16] H. Ding, P.D. Spelt, C. Shu, Diffuse interface model for incompressible two-phase flows with large density ratios, Journal of Computational Physics 226 (2007) 2078–2095.
[17] G. Tryggvason, S.O. Unverdi, Computations of three-dimensional Rayleigh–Taylor instability, Physics of Fluids A: Fluid Dynamics 2 (1990) 656–659.
[18] S.O. Unverdi, G. Tryggvason, Computations of multi-fluid flows, Physica D: Nonlinear Phenomena 60 (1992) 70–83.
[19] G. Tryggvason, B. Bunner, A. Esmaeeli, D. Juric, N. Al-Rawahi, W. Tauber, J. Han, S. Nas, Y.J. Jan, A front-tracking method for the computations of multiphase flow, Journal of Computational Physics 169 (2001) 708–759.
[20] S. Osher, J.A. Sethian, Fronts propagating with curvature-dependent speed: algorithms based on Hamilton–Jacobi formulations, Journal of Computational Physics 79 (1988) 12–49.

[21] M. Sussman, P. Smereka, S. Osher, A level set approach for computing solutions to incompressible two-phase flow, Journal of Computational Physics 114 (1994) 146–159.
[22] M. Herrmann, A balanced force refined level set grid method for two-phase flows on unstructured flow solver grids, Journal of Computational Physics 227 (2008) 2674–2706.
[23] O. Desjardins, V. Moureau, H. Pitsch, An accurate conservative level set/ghost fluid method for simulating turbulent atomization, Journal of Computational Physics 227 (2008) 8395–8416.
[24] R. Scardovelli, S. Zaleski, Direct numerical simulation of free-surface and interfacial flow, Annual Review of Fluid Mechanics 31 (1999) 567–603.
[25] T. Boeck, J. Li, E. Lopez-Pages, P. Yecko, S. Zaleski, Ligament formation in sheared liquid–gas layers, Theoretical and Computational Fluid Dynamics 21 (2007) 59–76.
[26] R. Nourgaliev, M.-S. Liou, T. Theofanous, Numerical prediction of interfacial instabilities: sharp interface method (sim), Journal of Computational Physics 227 (2008) 3940–3970.
[27] A. Bagué, D. Fuster, S. Popinet, R. Scardovelli, S. Zaleski, Instability growth rate of two-phase mixing layers from a linear eigenvalue problem and an initial-value problem, Physics of Fluids 22 (2010) 092104.
[28] D. Fuster, G. Agbaglah, C. Josserand, S. Popinet, S. Zaleski, Numerical simulation of droplets, bubbles and waves: state of the art, Fluid Dynamics Research 41 (2009) 065001.
[29] G. Tomar, D. Fuster, S. Zaleski, S. Popinet, Multiscale simulations of primary atomization, Computers and Fluids 39 (2010) 1864–1874.
[30] D. Fuster, A. Bagué, T. Boeck, L.L. Moyne, A. Leboissetier, S. Popinet, P. Ray, R. Scardovelli, S. Zaleski, Simulation of primary atomization with an octree adaptive mesh refinement and vof method, International Journal of Multiphase Flow 35 (2009) 550–565.
[31] F.P. Bertolotti, T. Herbert, P.R. Spalart, Linear and nonlinear stability of the Blasius boundary layer, Journal of Fluid Mechanics 242 (1992) 441–474.
[32] T. Herbert, Parabolized Stability Equations, Technical Report AGARD-R-793, Von Karman Institute, Rhode-Saint-Genese, 1994.
[33] T. Herbert, Parabolized stability equations, Annual Reviews of Fluid Mechanics 29 (1997) 245–283.
[34] M.J. Day, N.N. Mansour, W.C. Reynolds, Nonlinear stability and structure of compressible reacting mixing layers, Journal of Fluid Mechanics 446 (2001) 375–408.
[35] M.R. Malik, C.L. Chang, Nonparallel and nonlinear stability of supersonic jet flow, Computers and Fluids 29 (2000) 327–365.
[36] L.C. Cheung, S.K. Lele, Linear and non-linear processes in two-dimensional mixing layer dynamics and sound radiation, Journal of Fluid Mechanics 625 (2009) 321–351.
[37] F.M. White, Viscous Fluid Flow, McGraw-Hill, 1991.
[38] P. Huerre, P.A. Monkewitz, Local and global instabilities in spatially developing flows, Annual Reviews of Fluid Mechanics 22 (1990) 473–537.
[39] H. Haj-Hariri, Characteristics analysis of the parabolized stability equations, Studies of Applied Mathematics 92 (1994) 41–53.
[40] S.V. Malik, A.P. Hooper, Linear stability and energy growth of viscosity stratified flows, Physics of Fluids 17 (2005) 024101.
[41] S.J. Leib, M.E. Goldstein, The generation of capillary instabilities on a liquid jet, Journal of Fluid Mechanics 168 (1986) 479–500.
[42] S.J. Leib, M.E. Goldstein, Convective and absolute instability of a viscous liquid jet, Physics of Fluids 29 (1986) 952–954.
[43] S.J. Rees, M.P. Juniper, The effect of surface tension on the stability of unconfined and confined planar jets and wakes, Journal of Fluid Mechanics 633 (2009) 71–97.
[44] S.P. Lin, R.D. Reitz, Drop and spray formation from a liquid jet, Annual Review of Fluid Mechanics 30 (1998) 85–105.
[45] P. Marmottant, E. Villermaux, On spray formation, Journal of Fluid Mechanics 498 (2004) 73–111.
[46] J.C. Lasheras, E.J. Hopfinger, Liquid jet instability and atomization in a coaxial gas stream, Annual Review of Fluid Mechanics 32 (2000) 275–308.
[47] C.A.J. Fletcher, Computational Techniques for Fluid Dynamics 2, Springer-Verlag, Berlin, 1991.
[48] P. Andersson, D.S. Henningson, A. Hanifi, On a stabilization procedure for the parabolic stability equations, Journal of Engineering Mathematics 33 (1998) 311–332.
[49] F. Li, M.R. Malik, On the nature of the PSE approximation, Theoretical and Computational Fluid Dynamics 8 (1996) 253–273.
[50] E. Olsson, G. Kreiss, S. Zahedi, A conservative level set method for two phase flow ii, Journal of Computational Physics 225 (2007) 785–807.
[51] M. Rosenfeld, D. Kwak, M. Vinokur, A fractional step solution method for the unsteady incompressible Navier–Stokes equations in generalized coordinate systems, Journal of Computational Physics 94 (1991) 102–137.
[52] S. Saha, S.Y. Jung, T.A. Zaki, Stabilization of wall shear beneath vortical disturbances using a thin film, in: Seventh International Conference on Multiphase flows, Tampa, FL, May 30–June 4, 2010.
[53] C.M. Ho, P. Huerre, Perturbed free shear layers, Annual Reviews of Fluid Mechanics 16 (1984) 365–424.
[54] W. Tauber, S.O. Unverdi, G. Tryggvason, The nonlinear behavior of a sheared immiscible fluid interface, Physics of Fluids 14 (2002) 2871–2885.